The Astrophysical Journal, 700:309–330, 2009 July 20 doi:10.1088/0004-637X/700/1/309

EXTRAGALACTIC CHEMICAL ABUNDANCES: DO H II REGIONS AND YOUNG STARS TELL THE SAME STORY? THE CASE OF THE SPIRAL GALAXY NGC 300*

Fabio Bresolin[1], Wolfgang Gieren[2], Rolf-Peter Kudritzki[1], Grzegorz Pietrzyński[2,3], Miguel A. Urbaneja[1], and Giovanni Carraro[4]

[1] Institute for Astronomy, 2680 Woodlawn Drive, Honolulu, HI 96822, USA
[2] Universidad de Concepción, Departamento de Astronomia, Casilla 160-C, Concepción, Chile
[3] Warsaw University Observatory Al Ujazdowskie 4, 00-478 Warsaw, Poland
[4] European Southern Observatory, Alonso de Cordova 3107, Santiago, Chile
Received 2009 February 26; accepted 2009 May 19; published 2009 July 1

ABSTRACT

We have obtained new spectrophotometric data for 28 H II regions in the spiral galaxy NGC 300, a member of the nearby Sculptor Group. The detection of several auroral lines, including [O III] λ4363, [S III] λ6312, and [N II] λ5755, has allowed us to measure electron temperatures and direct chemical abundances for the whole sample. We determine for the first time in this galaxy a radial gas-phase oxygen abundance gradient based solely on auroral lines, and obtain the following least-square solution: $12 + \log(\mathrm{O/H}) = 8.57(\pm0.02) - 0.41(\pm0.03)R/R_{25}$, where the galactocentric distance is expressed in terms of the isophotal radius R_{25}. The characteristic oxygen abundance, measured at $0.4 \times R_{25}$, is $12 + \log(\mathrm{O/H}) = 8.41$. The gradient corresponds to -0.077 ± 0.006 dex kpc^{-1}, and agrees very well with the galactocentric trend in metallicity obtained for 29 B and A supergiants in the same galaxy, -0.081 ± 0.011 dex kpc^{-1}. The intercept of the regression for the nebular data virtually coincides with the intercept obtained from the stellar data, which is 8.59(±0.05). This allows little room for depletion of nebular oxygen onto dust grains, although in this kind of comparison we are somewhat limited by systematic uncertainties, such as those related to the atomic parameters used to derive the chemical compositions. We discuss the implications of our result with regard to strong-line abundance indicators commonly used to estimate the chemical compositions of star-forming galaxies, such as R_{23}. By applying a few popular calibrations of these indices based on grids of photoionization models on the NGC 300 H II region fluxes, we find metallicities that are higher by 0.3 dex (a factor of 2) or more relative to our nebular (T_e based) and stellar ones. We detect Wolf–Rayet stellar emission features in ∼1/3 of our H II region spectra, and find that in one of the nebulae hosting these hot stars the ionizing field has a particularly hard spectrum, as gauged by the "softness" parameter $\eta = (\mathrm{O^+/O^{++}})/(\mathrm{S^+/S^{++}})$. We suggest that this is related to the presence of an early WN star. By considering a larger sample of extragalactic H II regions we confirm, using direct abundance measurements, previous findings of a metallicity dependence of η, in the sense that softer stellar continua are found at high metallicity.

Key words: galaxies: abundances – galaxies: individual (NGC 300) – galaxies: ISM

Online-only material: color figures

1. INTRODUCTION

The spectral analysis of H II regions has been an invaluable tool in astrophysics for the past few decades, providing a straightforward means to measure present-day chemical abundances in a variety of galactic environments, which has led, for example, to the study of radial abundance gradients in spiral galaxies (Vila-Costas & Edmunds 1992; Zaritsky et al. 1994). It has recently become possible to extend the nebular techniques to star-forming galaxies at high redshift (Pettini et al. 2001; Shapley et al. 2004), allowing the investigation of cosmic chemical enrichment (Kobulnicky & Kewley 2004; Savaglio et al. 2005; Maier et al. 2006; Liu et al. 2008; Cowie & Barger 2008) in connection to fundamental properties of galaxies such as the mass–metallicity relation (Lequeux et al. 1979; Tremonti et al. 2004; Erb et al. 2006; Maiolino et al. 2008; Pérez-Montero et al. 2009).

The work on young massive stars to obtain reliable metallicities in nearby galaxies is less mature, due to the need for a sophisticated non-local thermodynamic equilibrium (NLTE) treatment of the physical processes involving millions of metal lines in expanding atmospheres (Hillier & Miller 1998; Pauldrach et al. 2001; Puls et al. 2005), and the requirement for telescopes with large collecting areas to secure spectra of individual stars located a few Mpc away (Bresolin et al. 2001, 2002a). While it is possible to measure stellar metallicities from the integrated spectra of young star clusters (Larsen et al. 2006, 2008) or for star-forming galaxies at high redshift (Rix et al. 2004; Halliday et al. 2008), more stringent tests that compare the chemical compositions of galaxies as obtained from H II regions and massive stars should be carried out in nearby, well resolved systems. In doing so, the comparison is limited to chemical elements that are measurable in both types of objects and that, contrary to nitrogen, are largely unaffected by rotational mixing (Maeder & Meynet 2000; Hunter et al. 2007). For these reasons, the abundances of oxygen, and more rarely iron, can be directly compared between ionized nebulae and young stars, mostly early-B dwarfs (within the Milky Way and in the Magellanic Clouds), and brighter A and B supergiants (in more distant galaxies). The expectation is that, once evolutionary effects in stars are properly accounted for, the present-day abundances derived from young massive stars and H II regions agree within the uncertainties of the measurements and of the modeling.

In low metallicity and generally chemically homogeneous galaxies, such as the Magellanic Clouds and a small number of dwarf irregulars of the Local Group, the agreement found

* Based on observations collected at the European Southern Observatory, Chile, under program 077.B-0269.

between H II region and young star chemical abundances is satisfactory (e.g., Trundle & Lennon 2005; Bresolin et al. 2006; Lee et al. 2006). The possibilities for comparison are even fewer in the case of spiral galaxies, as only data for the Milky Way (Rolleston et al. 2000; Deharveng et al. 2000; Daflon & Cunha 2004) and M33 (Vílchez et al. 1988; Urbaneja et al. 2005a; Magrini et al. 2007; Rosolowsky & Simon 2008) have insofar allowed meaningful comparisons. Yet, these are perhaps the most interesting cases, because the metallicity in spiral galaxies can span a wide range, from the metal-rich nuclear regions to the metal-poor outskirts, of up to 1 dex (as in the case of M101; Kennicutt et al. 2003).

A well documented complication in H II region studies arises as the metallicity approaches the solar one (we adopt $12+\log(\mathrm{O/H})_\odot = 8.66$ from Asplund et al. 2005). The classical method of nebular abundance analysis is based on the measurement of the [O III] λ4363/ λ5007 line ratio, which is highly sensitive to the electron temperature of the gas, upon which the line emissivities strongly depend. As the nebular cooling shifts from optical to IR transitions with increasing metallicity (for example, approaching the centers of spiral galaxies), the auroral line [O III] λ4363 becomes extremely faint, and virtually unobservable in extragalactic H II regions near the solar metallicity, except for the brightest objects. The common solution is to base the abundance measurements on line ratios that involve the strongest collisionally excited lines that are present in nebular spectra, such as R_{23} = ([O II] λ3727+[O III] λλ4959,5007)/Hβ (Pagel et al. 1979). However, the use of these techniques is not exempt from difficulties, and in particular different calibrations of "strong-line indices" in terms of the oxygen abundance lead to poorly understood systematic discrepancies (Bresolin 2008; Kewley & Ellison 2008). Alternatively, deep observations aimed at the detection of [O III] λ4363 or other auroral lines, such as [S III] λ6312 and [N II] λ5575, can be carried out to by-pass these calibration issues, in order to have a "direct" measurement of the chemical abundances from the knowledge of the electron temperature T_e, as done recently by our group (Kennicutt et al. 2003; Garnett et al. 2004; Bresolin et al. 2004, 2005). Although this approach is potentially prone to systematic errors due to the effects of temperature gradients within the nebulae at high abundance (Stasińska 2005), the data suggest that the direct abundances are reliable at least up to the solar value (Bresolin 2007).

A further issue in nebular astrophysics is represented by the so-called abundance discrepancy, consisting of the fact that when O II recombination lines are used to determine O^{++} abundances in place of the much stronger [O III] collisionally excited lines, the resulting total oxygen abundances are larger, by 0.2 dex on average (García-Rojas & Esteban 2007). The effect is measured in Galactic H II regions, ionized by one or few stars, such as the Orion Nebula, M8 and M17 (Esteban et al. 2004; García-Rojas et al. 2007), as well as in more luminous extragalactic H II regions, such as 30 Dor in the Large Magellanic Cloud (LMC; Peimbert 2003), NGC 604 in M33 and others (Esteban et al. 2002, 2009). As shown by García-Rojas & Esteban (2007), the effect does not seem to depend on metallicity or other nebular parameters, and can be interpreted with the presence of temperature fluctuations in H II regions (Peimbert 1967). The size of the discrepancy is large enough that it would affect the comparison between nebular and stellar abundances in such a way that it should be possible to discern which nebular abundance determination method best agrees with the stellar measurements.

Table 1
NGC 300: Galaxy Parameters

Parameter	Value
R.A. (J2000.0)	00:54:53.48
Decl. (J2000.0)	−37:41:03.8
Morphological type	Scd
Distance	1.88 Mpc[a]
R_{25}	9.′75 (5.33 kpc)
Inclination	39.°8
Position angle of major axis	114.°3
Heliocentric radial velocity	144 km s^{-1}
B_T^0	8.49[b]
M_B^0	−17.88

Notes. All parameters from the HyperLeda database (Paturel et al. 2003), except where noted. M_B^0 calculated from B_T^0 and the adopted distance.
[a] Gieren et al. (2005).
[b] de Vaucouleurs et al. (1991).

In this paper, we reassess the issue of present-day chemical abundances determined jointly from H II regions and massive stars by analyzing new H II region spectroscopy obtained in the southern spiral galaxy NGC 300. This Scd galaxy is located in the Sculptor Group at a Cepheid distance of 1.88 Mpc (Gieren et al. 2005). Table 1 summarizes some essential parameters of this galaxy. Its proximity has made it the subject of a number of investigations during the past decade concerning the stellar populations in the central/nuclear regions (Davidge 1998; Walcher et al. 2006) and in the outskirts (Tikhonov et al. 2005; Bland-Hawthorn et al. 2005; Mouhcine 2006; Vlajić et al. 2009), the star formation history (Butler et al. 2004), Wolf–Rayet (W–R) stars and OB associations (Schild et al. 2003; Pietrzyński et al. 2001), planetary nebulae (Soffner et al. 1996; M. Peña et al. 2009, in preparation), variable stars (Pietrzyński et al. 2002; Mennickent et al. 2004), dust content (Helou et al. 2004; Roussel et al. 2005), X-ray sources (Read & Pietsch 2001; Carpano et al. 2005), supernova remnants (SNRs; Blair & Long 1997; Pannuti et al. 2000; Payne et al. 2004), and UV emission properties (Muñoz-Mateos et al. 2007).

Spectroscopic work on the blue supergiants of NGC 300 has recently been carried out by our group. Following the spectral classification of nearly 70 stars by Bresolin et al. (2002a), Urbaneja et al. (2005b) measured O, Mg, and Si abundances for six early-B supergiants, while Kudritzki et al. (2008) derived metallicities for 24 B8–A4 supergiants. H II region abundances have been first measured by Pagel et al. (1979) in their seminal paper that introduced the R_{23} abundance indicator. Subsequent abundance studies were carried out by Webster & Smith (1983), Edmunds & Pagel (1984), Deharveng et al. (1988), and Christensen et al. (1997). Additional nebular spectroscopic work includes various searches for W–R stars (D'Odorico et al. 1983; Schild & Testor 1992; Schild et al. 2003, among others), and the search for SNRs by Blair & Long (1997). Deharveng et al. (1988) presented a catalog of 176 H II regions in NGC 300, superseding a previous one by Sérsic (1966), and discussed the radial abundance gradient from a compilation of new and previously published spectral data for 28 H II regions.

Despite all of these studies, until now only two H II regions in NGC 300 had a direct, [O III] λ4363-based determination of the oxygen abundance (one each in Pagel et al. 1979 and Webster & Smith 1983), limiting considerably the accuracy with which the metallicity gradient is known for this galaxy. The availability

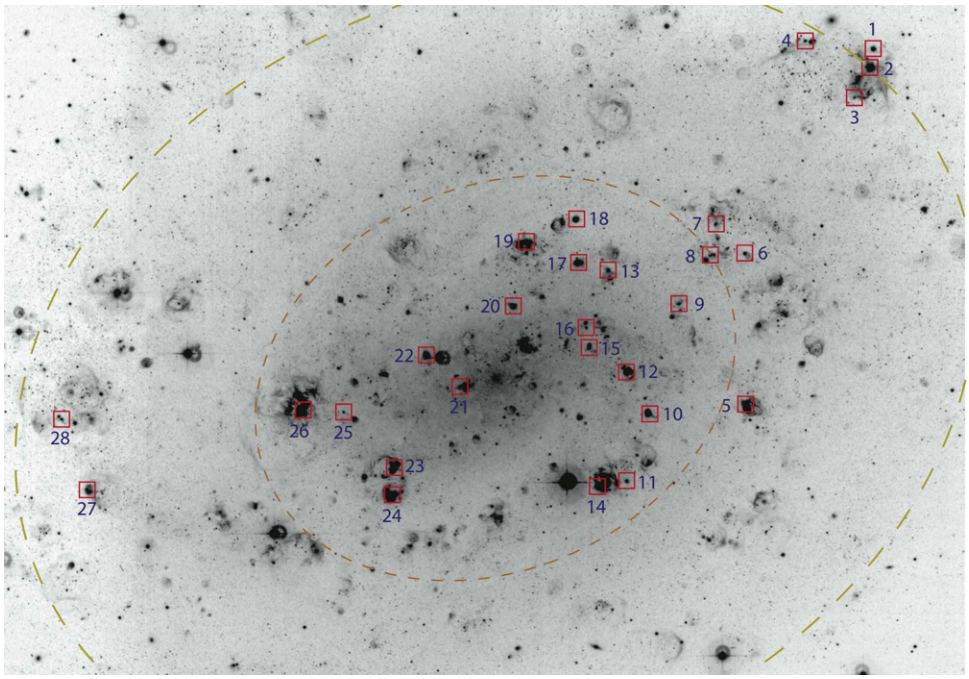

Figure 1. Location of the H II regions studied in this work on a narrowband Hα image of NGC 300 (courtesy ESO). The H II regions are numbered in the order of increasing right ascension. The dashed lines represent the location of the projected 0.5 R_{25} and R_{25} radii ($R_{25} = 9.'75$).

(A color version of this figure is available in the online journal.)

of metallicity determinations for a large number of stars in NGC 300 (Urbaneja et al. 2005b; Kudritzki et al. 2008) provided the motivation to carry out a modern re-evaluation of the nebular abundances in this galaxy, with the goal of measuring high-quality, direct abundances from the detection of the auroral lines. The data presented here allow a new comparison between stellar and T_e-based H II region abundances, only the third of its kind for a spiral galaxy, after the Milky Way and M33. As we will show, this kind of comparisons has important implications, for example, concerning the calibration of strong-line abundance methods.

Our paper is organized as follows: the new observations and the data reduction are presented in Section 2, followed by the determination of electron temperatures of the ionized gas from the auroral lines in Section 3. Chemical abundances are derived in Section 4, and we discuss the abundance gradient in NGC 300, comparing H II regions with young stars, in Section 5. The discussion in Section 6 focuses on results of similar comparisons in other galaxies, and presents comments on the strong-line methods, the W–R star content, and the properties of the ionizing radiation in a wider sample of H II regions. We summarize our main results in Section 7.

2. OBSERVATIONS AND DATA REDUCTION

Multi-object spectroscopy of H II regions in NGC 300 was obtained on the nights of 2006 August 17 and 18 at the Very Large Telescope (VLT) of the European Southern Observatory (ESO) on Cerro Paranal. The FORS2 instrument was used with 1 arcsec slits to cover targets in three different $6.'8 \times 6.'8$ regions of the galaxy, located near the galactic center (with two separate multi-object setups), as well as east and northwest of the center (one setup each). The targets had been selected from narrowband Hα images obtained on 2006 July 1 with the same instrument. The sky conditions were clear, and the seeing varied between 0.5 and 0.9 arcsec during most of the observing run (the seeing was 1.3 arcsec at the end of the run, while observing additional H II regions in the central field).

Because of the requirement of covering a fairly extended wavelength range (from [O II] λ3727 to [S III] $\lambda\lambda$9069,9532) at a moderate spectral resolution (5–10 Å), we combined each object mask with three different grisms: 600B (4×1800 s exposures, approximate range: 3500–6000 Å for a slit located near the center of the detector, 4.5 Å FWHM spectral resolution), 600R (4×1800 s, approximate range: 5300–8300 Å, 5 Å resolution), and 300I (2×900 s, approximate range: 6100–10000 Å, 10 Å resolution).

The first stages of the data reduction, including bias subtraction, flat-field correction, and wavelength calibration, were carried out with the EsoRex pipeline provided by the ESO. Cosmic rays were removed with the L.A.Cosmic routine (van Dokkum 2001), while standard IRAF[5] tasks were used for the spectral extractions, image co-additions, and flux calibration (we obtained spectra of the spectrophotometric standards BPM 16274, EG 21, EG 274, LDS 749B and NGC 7293).

Since in this paper we focus on direct measurements of the H II region chemical abundances, without relying on statistical abundance indicators, we limit our discussion to the 28 targets for which we could measure reliable electron temperatures from auroral-to-nebular line ratios, with the methods explained in Section 3. The spatial distribution of this sample is shown in Figure 1, while the celestial coordinates of the targets and their identification from previous studies are summarized in Table 2. The positions were measured on an Hα image taken by FB in 2000 August at the MPG/ESO 2.2 m telescope on La Silla, equipped with the Wide Field Imager. The rms uncertainty of the astrometric solution, derived using stars in the USNO catalog, is 0.4 arcsec.

[5] IRAF is distributed by the National Optical Astronomy Observatories, which is operated by the Association of Universities for Research in Astronomy, Inc., under cooperative agreement with the National Science Foundation.

Table 2
H II Region Sample

ID	R.A. (J2000.0)	Decl. (J2000.0)	R/R_{25}	ID
(1)	(2)	(3)	(4)	(5)
1	00 54 16.22	−37 34 35.9	1.03	5 (W 16)
2	00 54 16.28	−37 34 54.9	1.01	6 (P 7; W 14-15; D 1)
3	00 54 17.98	−37 35 33.2	0.93	...
4	00 54 22.83	−37 34 25.9	0.97	12
5	00 54 28.70	−37 41 32.8	0.55	24 (W 11; D 2; S 13)
6	00 54 28.83	−37 38 36.3	0.56	25
7	00 54 31.70	−37 38 01.5	0.55	30
8	00 54 32.20	−37 38 37.7	0.50	32 (S 19)
9	00 54 35.35	−37 39 35.3	0.40	37
10	00 54 38.16	−37 41 44.8	0.36	39 (S 21)
11	00 54 40.53	−37 43 03.1	0.41	46 (S 23)
12	00 54 40.56	−37 40 55.3	0.27	45 (W 4; D 3)
13	00 54 42.29	−37 38 56.1	0.33	50
14	00 54 43.42	−37 43 09.3	0.38	53A (P 5; W 5; D 6; S 29)
15	00 54 44.22	−37 40 25.7	0.20	56
16	00 54 44.52	−37 40 03.1	0.21	58
17	00 54 45.28	−37 38 46.5	0.31	61 (S 31)
18	00 54 45.37	−37 37 56.1	0.41	63
19	00 54 50.34	−37 38 22.6	0.34	77 (P 1; D 7; S 38)
20	00 54 51.69	−37 39 38.7	0.18	84 (S 41)
21	00 54 57.02	−37 41 12.4	0.08	...
22	00 55 00.38	−37 40 35.4	0.17	109 (P 2; D 9; S 53)
23	00 55 03.56	−37 42 48.5	0.28	118A (D 11; S 59)
24	00 55 03.65	−37 43 19.4	0.33	119A (W 6; D 12; S 58)
25	00 55 08.53	−37 41 42.3	0.32	128
26	00 55 12.58	−37 41 39.2	0.40	137A (W 7; D 14)
27	00 55 33.94	−37 43 12.8	0.86	159 (P 4; S 80)
28	00 55 36.45	−37 41 49.7	0.91	161

Notes. Units of right ascension are hours, minutes, and seconds, and units of declination are degrees, arcminutes, and arcseconds. Column 1: H II region identification; Column 2: right ascension; Column 3: declination; Column 4: galactocentric distance in units of $R_{25} = 9.75$ arcmin; Column 5: identification from Deharveng et al. 1988. Additional IDs in brackets—P: Pagel et al. 1979; Edmunds & Pagel 1984; W: Webster & Smith 1983; D: D'Odorico et al. 1983; S: Sérsic 1966.

The deprojected galactocentric distances in Column 4 are given in terms of the 25th magnitude B-band isophotal radius, $R_{25} = 9\farcm75$ (=5.33 kpc at the adopted distance of 1.88 Mpc), and were calculated adopting the disk parameters reported in Table 1. As Table 2 shows, almost all of our targets are included in the catalog compiled by Deharveng et al. (1988; entries from this catalog will be indicated with the prefix De). The only exceptions are our objects No. 3 and No. 21, both rather compact H II regions (No. 21 could be the eastern extension of what Deharveng et al. 1988 considered as a single object, De 100 in their catalog).

The reddening-corrected emission lines presented in Tables 3 and 4 were measured with the `splot` task in IRAF. The reddening correction was obtained with an iterative procedure from the Balmer decrement, assuming case B H I line ratios (Hummer & Storey 1987), calculated at the electron temperatures derived from the auroral lines, simultaneously determining the correction for the underlying stellar absorption. The interstellar reddening law of Seaton (1979) has been adopted. The internal consistency of the flux calibration in the blue was checked by ensuring that the strengths of the higher order lines of the Balmer series that are still measurable in our spectra (H9–H11) agree, within the errors, with the case B predictions.

The line flux errors were calculated using the expression by González-Delgado et al. (1994)

$$\sigma_l = \sigma_{\rm cont}\, N^{1/2}\, [1 + {\rm EW}/(N\Delta)]^{1/2}, \quad (1)$$

where $\sigma_{\rm cont}$ is the standard deviation of the continuum near the emission line, N is the width of the region used to measure the line in pixels, Δ is the spectral dispersion in Å pixel^{-1}, and EW represents the equivalent width of the line. The final errors quoted in Tables 3 and 4 include, added in quadrature, contributions of 1% and 4% due to the uncertainties in the flat fielding and the flux calibration, respectively, as well as the uncertainty in scaling spectra obtained through different grisms (estimated to be 3%). In propagating the errors, we also accounted for the uncertainty in the extinction coefficient $c(\mathrm{H}\beta)$, which amounts to about 0.07 mag. The Hβ line flux that appears in Column 9 of Table 4 has been corrected for extinction, and should be regarded as a lower limit of the real flux, due to slit losses. The missing entries for the He I λ5876 and/or [S III] λ6312 lines are due to the fact that the 600R grism introduces a shift along the spatial direction, so that spectra near the top edge of the two 2048 × 2048 FORS2 detectors cannot be recorded. In one case [N II] λ5755 is also missing, because the line could not be measured in the blue (600B) spectra, while in all of the remaining targets this line was measured in either the red (600R) or the blue spectra, or in both.

Only one of our targets, No. 27 (=De 159), appears in the list of optically selected SNRs by Blair & Long (1997) as their source NGC 300-S28. We detect a modest [O I] λλ6300,6360 emission ([O I]/Hα = 0.04), but the shock excitation diagnostic line ratios [O I]/Hα and [S II]/Hα that we measure are 3 and 2.5 times smaller than the Blair & Long's (1997) values, respectively. We find [S II]/Hα = 0.29, considerably smaller than the minimum value of 0.4 commonly adopted in SNR searches to discriminate against photoionized nebulae, but this is also the largest [S II]/Hα ratio in our sample. This H II region appears as being composed of two separate bright knots, so it is likely that the object centered in our slit does not correspond to the one observed by Blair & Long (1997). In fact, while we do detect a few faint emission lines, such as [Mg I] λ4562 and [Fe III] λ4658 and λ5270, found in the spectra of SNRs (e.g., Osterbrock & Dufour 1973), this spectrum would not be flagged as that of an SNR on the basis of an [S II]/Hα versus [N II]/Hα diagnostic diagram (Sabbadin et al. 1977). We conclude that the SNR spectrum is fairly diluted by the H II region spectrum, and we keep this target in our analysis. A number of additional SNRs within H II regions have been discovered in NGC 300 with radio continuum observations by Pannuti et al. (2000) and Payne et al. (2004). Among these are several H II regions in our sample (D39, D53A, D61, D77, D84, D109, D118A, D119A, D137A, and D159). From our line ratios, we do not find evidence for significant shock excitation in these targets.

3. ELECTRON TEMPERATURES

The knowledge of the electron temperature of H II regions is crucial to obtain reliable nebular chemical abundances, because of the exponential temperature dependence of the line emissivity. In typical extragalactic work, the most common auroral line used for T_e determinations, [O III] λ4363, becomes very weak at moderately large oxygen abundance, as a result of the increasing cooling of the gas with metallicity. Somewhat surprisingly, the only previous detections of this line in NGC 300 are those in region 7 of Pagel et al. (1979; our region

Table 3
Reddening-corrected Fluxes (A)

ID	[O II] 3727	[Ne III] 3868	[S II] 4072	[O III] 4363	[O III] 5007	[N II] 5755	He I 5876	[S III] 6312	[N II] 6583
(1)	(2)	(3)	(4)	(5)	(6)	(7)	(8)	(9)	(10)
1	243 ± 17	20.6 ± 1.4	2.31 ± 0.23	3.38 ± 0.24	321 ± 19	...	...	...	13.5 ± 0.9
2	166 ± 12	33.8 ± 2.3	1.39 ± 0.11	5.59 ± 0.35	504 ± 29	0.18 ± 0.03	12.5 ± 0.8	1.85 ± 0.13	7.7 ± 0.5
3	373 ± 27	4.6 ± 0.5	3.46 ± 0.37	1.16 ± 0.19	119 ± 7	0.00 ± 0.15	11.5 ± 0.8	0.00 ± 0.11	23.4 ± 1.6
4	286 ± 20	14.9 ± 1.0	2.20 ± 0.19	2.14 ± 0.17	253 ± 15	0.00 ± 0.12	13.0 ± 0.8	1.73 ± 0.16	20.4 ± 1.3
5	296 ± 21	10.2 ± 1.1	3.25 ± 0.42	1.10 ± 0.15	226 ± 13	0.00 ± 0.08	11.9 ± 0.8	1.34 ± 0.16	29.7 ± 2.0
6	275 ± 20	13.9 ± 1.0	3.23 ± 0.25	1.16 ± 0.14	246 ± 14	0.00 ± 0.12	13.2 ± 0.9	1.38 ± 0.16	27.2 ± 1.8
7	134 ± 10	75.1 ± 5.3	3.64 ± 0.27	9.07 ± 0.59	908 ± 53	0.00 ± 0.08	...	...	15.6 ± 1.1
8	307 ± 22	7.2 ± 0.6	2.23 ± 0.17	0.77 ± 0.10	144 ± 8	0.50 ± 0.08	12.1 ± 0.8	1.32 ± 0.12	34.1 ± 2.2
9	172 ± 12	12.0 ± 0.8	1.95 ± 0.15	0.89 ± 0.08	235 ± 14	0.00 ± 0.04	13.1 ± 0.8	1.09 ± 0.08	32.5 ± 2.1
10	180 ± 13	13.1 ± 0.9	1.13 ± 0.09	0.91 ± 0.07	236 ± 14	0.23 ± 0.02	11.0 ± 0.7	1.11 ± 0.08	19.2 ± 1.3
11	258 ± 19	10.0 ± 0.7	2.74 ± 0.26	1.11 ± 0.18	201 ± 12	0.00 ± 0.07	11.5 ± 0.8	1.34 ± 0.12	29.3 ± 1.9
12	262 ± 19	0.0 ± 0.2	2.80 ± 0.25	0.00 ± 0.11	30 ± 2	0.37 ± 0.09	8.6 ± 0.6	0.73 ± 0.07	54.1 ± 3.5
13	246 ± 18	3.9 ± 0.3	2.06 ± 0.38	0.00 ± 0.21	119 ± 7	0.63 ± 0.08	13.1 ± 0.9	1.04 ± 0.09	40.2 ± 2.6
14	248 ± 18	8.1 ± 0.6	1.78 ± 0.12	0.75 ± 0.06	181 ± 11	0.40 ± 0.03	11.6 ± 0.8	1.40 ± 0.10	41.1 ± 2.7
15	185 ± 13	2.6 ± 0.2	2.22 ± 0.19	0.00 ± 0.11	92 ± 5	0.57 ± 0.11	12.5 ± 0.8	1.10 ± 0.10	58.1 ± 3.8
16	264 ± 19	3.4 ± 0.3	3.93 ± 0.30	0.00 ± 0.34	95 ± 6	0.69 ± 0.14	11.2 ± 0.8	0.99 ± 0.12	54.1 ± 3.6
17	213 ± 15	6.6 ± 0.5	1.29 ± 0.09	0.59 ± 0.05	192 ± 11	0.34 ± 0.04	13.6 ± 0.9	1.32 ± 0.11	27.6 ± 1.8
18	259 ± 18	4.6 ± 0.3	2.10 ± 0.17	0.00 ± 0.10	118 ± 7	0.41 ± 0.06	11.1 ± 0.7	1.26 ± 0.10	46.8 ± 3.1
19	192 ± 14	6.8 ± 0.5	2.17 ± 0.26	0.61 ± 0.05	165 ± 10	0.25 ± 0.03	15.0 ± 1.0	0.95 ± 0.07	23.3 ± 1.5
20	146 ± 10	9.9 ± 0.7	1.15 ± 0.09	0.71 ± 0.06	227 ± 13	0.28 ± 0.03	12.8 ± 0.8	1.15 ± 0.08	23.9 ± 1.6
21	217 ± 16	3.3 ± 0.4	3.42 ± 0.31	0.00 ± 0.09	103 ± 6	0.63 ± 0.08	9.6 ± 0.7	1.09 ± 0.12	72.7 ± 4.8
22	270 ± 19	3.3 ± 0.3	3.42 ± 0.34	0.00 ± 0.16	77 ± 4	0.47 ± 0.06	10.6 ± 0.7	0.82 ± 0.08	61.5 ± 4.0
23	176 ± 13	9.8 ± 0.7	1.61 ± 0.13	0.57 ± 0.07	198 ± 12	0.28 ± 0.02	11.7 ± 0.8	0.99 ± 0.09	27.8 ± 1.8
24	197 ± 14	5.2 ± 0.4	1.12 ± 0.11	0.62 ± 0.05	180 ± 10	0.37 ± 0.03	12.6 ± 0.8	...	32.4 ± 2.1
25	287 ± 21	4.2 ± 0.3	2.15 ± 0.20	0.00 ± 0.26	133 ± 8	0.60 ± 0.12	10.4 ± 0.7	1.07 ± 0.13	44.0 ± 2.9
26	160 ± 11	11.2 ± 0.8	1.77 ± 0.16	1.19 ± 0.10	259 ± 15	0.27 ± 0.03	12.2 ± 0.8	1.43 ± 0.10	20.3 ± 1.3
27	357 ± 25	9.8 ± 0.7	5.44 ± 0.36	1.59 ± 0.11	178 ± 10	0.54 ± 0.07	12.2 ± 0.8	1.50 ± 0.11	31.8 ± 2.1
28	314 ± 22	12.7 ± 0.9	2.04 ± 0.15	1.89 ± 0.13	244 ± 14	0.43 ± 0.10	11.8 ± 0.8	1.51 ± 0.19	21.3 ± 1.4

Note. The line fluxes are in units of Hβ = 100.

2 = De 6) and in region 7 of Webster & Smith (1983; our region 26 = De 137A). Our much deeper spectra allowed us to detect [O III] λ4363 in 20 H II regions. Moreover, it has been shown that for faint extragalactic H II regions the auroral lines of other ions, in particular [S III] λ6312 and [N II] λ5755, can be used as surrogates of [O III] λ4363 when the latter is not detected, especially at gas metallicities approaching the solar one (Bresolin et al. 2004, 2005), albeit the derived electron temperatures and chemical abundances are somewhat model dependent, and carry larger uncertainties. We have detected the [S III] λ6312 auroral line in eight additional objects, and we derived electron temperatures for the O^{++}-emitting region from this line, as explained below.

In the analysis of extragalactic H II regions, it is customary to assume a nebular structure that is described by a two- or a three-zone representation. Each zone is defined by an electron temperature, at which specific ions are found to be the dominant emitting species. In this paper, we assume a three-zone representation, characterized by the temperatures $T(O^{++})$, $T(S^{++})$, and $T(O^{+})$, in order of decreasing ionization potential of the ions that provide suitable emission lines for the temperature measurement. We assume that $T(O^{++})$ is the temperature at which the [O III] and [Ne III] lines are emitted (=T[O III]), and which is derived from the [O III] λ4363/ λλ4959,5007 line ratio. The ions [S III] and [Ar III] are assumed to be found at the temperature $T(S^{++})$, which is measured as T[S III] from the [S III] λ6312/ λλ9069,9532 line ratio. Finally, the lower excitation ions [O II], [S II], and [N II] are found in the zone characterized by $T(O^{+})$, which is typically measured as T[O II] from [O II] λ7325/ λ3727. Alternatively, one could also measure $T(O^{+})$ from nitrogen or sulfur lines, using the [N II] λ5755/ λλ6548,6583 and [S II] λ4072/ λλ6717,6731 auroral-to-nebular line ratios. Photoionization models predict correlations between the temperatures of the different zones (Stasińska 1982, 1990; Campbell et al. 1986; Garnett 1992; Pérez-Montero & Díaz 2003; Izotov et al. 2006, Pilyugin 2007). This is often exploited to infer the line temperature for ions that are not detected in nebular spectra.

We have derived electron temperatures T_e from the different line ratios mentioned in the previous paragraph, using the *temden* program (De Robertis et al. 1987), implemented in IRAF's *nebular* package (Shaw & Dufour 1995). We updated most of the atomic parameters used by the code, adopting collisional strengths and transition probabilities from recent sources in the literature, and summarized in Table 5 for the ions of interest. The electron densities N_e presented in Column 7 of Table 6 were derived iteratively as a function of T_e with *temden* from the [S II] λ6717/[S II] λ6731 line ratios. At very low densities (λ6717/ λ6731 approaching its maximum theoretical limit), we set $N_e = 20$ cm^{-3}.

In Figure 2, we plot the relationships between T[O III] and T[S III] (top), T[N II] (middle), and T[O II] (bottom). We include for comparison the correlations predicted by photoionization models: Garnett (1992, G92), Pérez-Montero & Díaz (2005, P05), Izotov et al. (2006, I06; their highest metallicity bin), and Stasińska (1990, S90), using for the latter the fits provided by Izotov et al. (1994). The top panel shows a tight correlation between T[O III] and T[S III], confirming earlier empirical

Table 4
Reddening-corrected Fluxes (B)

ID	He I 6678	[S II] 6717 + 6731	[Ar III] 7135	[O II] 7325	H I 9015	[S III] 9069	H I 9229	$F(H\beta)$ (erg s^{-1} cm^{-2})	$c(H\beta)$ (mag)
(1)	(2)	(3)	(4)	(5)	(6)	(7)	(8)	(9)	(10)
1	2.9 ± 0.2	22.1 ± 1.0	7.3 ± 0.5	6.1 ± 0.4	1.9 ± 0.2	17.0 ± 1.1	2.7 ± 0.2	7.6×10^{-15}	0.23
2	3.1 ± 0.2	17.4 ± 0.8	8.7 ± 0.6	4.3 ± 0.3	1.9 ± 0.1	19.6 ± 1.3	2.5 ± 0.2	8.7×10^{-15}	0.12
3	2.8 ± 0.2	52.0 ± 2.5	5.3 ± 0.4	8.0 ± 0.6	2.3 ± 0.2	12.7 ± 0.9	2.5 ± 0.2	1.0×10^{-15}	0.03
4	3.9 ± 0.3	33.2 ± 1.6	9.2 ± 0.6	6.0 ± 0.4	1.7 ± 0.1	20.7 ± 1.4	2.5 ± 0.2	6.5×10^{-15}	0.40
5	3.3 ± 0.2	52.7 ± 2.5	8.8 ± 0.6	4.7 ± 0.3	2.0 ± 0.1	26.4 ± 1.7	2.5 ± 0.2	6.9×10^{-15}	0.15
6	3.3 ± 0.2	38.6 ± 1.8	8.7 ± 0.6	4.1 ± 0.4	2.0 ± 0.2	20.3 ± 1.4	2.5 ± 0.2	4.7×10^{-15}	0.25
7	3.1 ± 0.3	34.9 ± 1.7	14.7 ± 1.0	3.8 ± 0.3	1.7 ± 0.2	30.9 ± 2.1	2.7 ± 0.2	2.7×10^{-15}	0.00
8	3.1 ± 0.2	44.2 ± 2.1	7.9 ± 0.5	4.4 ± 0.3	1.8 ± 0.1	20.6 ± 1.4	2.6 ± 0.2	7.6×10^{-15}	0.34
9	3.5 ± 0.2	33.1 ± 1.5	10.3 ± 0.7	3.2 ± 0.2	1.9 ± 0.1	27.2 ± 1.8	2.6 ± 0.2	7.2×10^{-15}	0.33
10	3.0 ± 0.2	16.3 ± 0.8	9.5 ± 0.6	2.2 ± 0.2	1.7 ± 0.1	26.5 ± 1.7	2.6 ± 0.2	42.0×10^{-15}	0.72
11	3.5 ± 0.2	41.8 ± 2.0	10.7 ± 0.7	5.6 ± 0.4	2.2 ± 0.2	23.8 ± 1.6	2.5 ± 0.2	6.6×10^{-15}	0.20
12	2.5 ± 0.2	72.5 ± 3.4	4.6 ± 0.3	2.8 ± 0.2	2.1 ± 0.1	22.0 ± 1.4	2.6 ± 0.2	9.1×10^{-15}	0.17
13	2.9 ± 0.2	37.5 ± 1.8	6.7 ± 0.4	2.8 ± 0.2	1.8 ± 0.1	21.2 ± 1.4	2.6 ± 0.2	9.0×10^{-15}	0.43
14	3.8 ± 0.2	41.6 ± 1.9	12.1 ± 0.8	4.7 ± 0.3	2.0 ± 0.1	29.6 ± 1.9	2.6 ± 0.2	48.5×10^{-15}	0.17
15	3.5 ± 0.2	48.0 ± 2.3	9.0 ± 0.6	3.0 ± 0.2	1.9 ± 0.1	28.1 ± 1.8	2.6 ± 0.2	17.1×10^{-15}	0.43
16	3.1 ± 0.2	53.0 ± 2.5	8.3 ± 0.6	3.8 ± 0.3	2.1 ± 0.2	24.3 ± 1.6	2.6 ± 0.2	6.9×10^{-15}	0.50
17	3.3 ± 0.2	27.3 ± 1.3	8.8 ± 0.6	2.3 ± 0.2	1.9 ± 0.1	27.3 ± 1.8	2.6 ± 0.2	22.5×10^{-15}	0.28
18	3.6 ± 0.2	57.2 ± 2.7	10.6 ± 0.7	5.2 ± 0.4	1.6 ± 0.1	25.9 ± 1.7	2.6 ± 0.3	9.0×10^{-15}	0.13
19	3.8 ± 0.2	30.6 ± 1.4	6.3 ± 0.4	2.1 ± 0.1	2.0 ± 0.1	23.1 ± 1.5	2.6 ± 0.2	31.2×10^{-15}	0.24
20	3.6 ± 0.2	20.0 ± 0.9	10.8 ± 0.7	2.3 ± 0.2	1.9 ± 0.1	28.6 ± 1.9	2.5 ± 0.2	44.1×10^{-15}	0.33
21	3.0 ± 0.2	55.5 ± 2.6	10.2 ± 0.7	3.5 ± 0.3	1.8 ± 0.2	28.8 ± 1.9	2.6 ± 0.2	11.1×10^{-15}	0.76
22	3.0 ± 0.2	71.6 ± 3.3	7.6 ± 0.5	3.7 ± 0.3	1.9 ± 0.1	22.3 ± 1.5	2.5 ± 0.2	8.3×10^{-15}	0.29
23	3.4 ± 0.2	28.0 ± 1.3	10.5 ± 0.7	3.0 ± 0.2	2.0 ± 0.1	24.0 ± 1.6	2.5 ± 0.2	45.0×10^{-15}	0.31
24	2.9 ± 0.2	30.3 ± 1.4	9.3 ± 0.6	3.6 ± 0.2	2.1 ± 0.1	26.5 ± 1.7	2.6 ± 0.2	27.5×10^{-15}	0.04
25	3.4 ± 0.2	45.0 ± 2.1	10.7 ± 0.7	5.7 ± 0.4	2.3 ± 0.2	24.6 ± 1.6	2.6 ± 0.2	8.4×10^{-15}	0.47
26	3.7 ± 0.2	22.1 ± 1.0	11.4 ± 0.7	3.2 ± 0.2	1.7 ± 0.1	28.2 ± 1.8	2.5 ± 0.2	30.5×10^{-15}	0.33
27	2.7 ± 0.2	81.7 ± 3.8	6.4 ± 0.4	6.0 ± 0.4	1.3 ± 0.1	17.3 ± 1.1	2.6 ± 0.2	7.7×10^{-15}	0.22
28	4.2 ± 0.2	37.2 ± 1.7	7.8 ± 0.6	6.0 ± 0.4	1.7 ± 0.1	21.2 ± 1.4	2.7 ± 0.2	4.0×10^{-15}	0.16

Note. The line fluxes are in units of $H\beta = 100$.

Table 5
Sources of Atomic Data

Ion	Transition Probabilities	Collision Strengths
[O II]	Froese Fischer & Tachiev (2004)[a]	Tayal (2007)[a]
[O III]	Froese Fischer & Tachiev (2004)[a]	Aggarwal & Keenan (1999)[a]
[N II]	Froese Fischer & Tachiev (2004)[a]	Hudson & Bell (2005)[a]
[Ne III]	Froese Fischer & Tachiev (2004)[a]	McLaughlin & Bell (2000)[a]
[Ar III]	Mendoza (1983) Kaufman & Sugar (1986)	Galavis et al. (1995)
[S II]	Froese Fischer et al. (2006)[a]	Ramsbottom et al. (1996)
[S III]	Froese Fischer et al. (2006)[a]	Tayal & Gupta (1999)[a]

Note.
[a] Updated from IRAF's value.

measurements in H II regions within M101 by Kennicutt et al. (2003). The rms deviations of the data points from the model predictions of Garnett (1992, full red line) and Izotov et al. (2006, black dotted curve) are comparable (410 K versus 470 K), while the models by Pérez-Montero & Díaz (2005) provide a slightly worse fit to the data (the scatter around their model line is 560 K).

In the case of T[N II] versus T[O III] (Figure 2, middle), a clear correlation is also seen, but the fit to the model predictions is not as good as in the T[S III] case. Formally, the Izotov et al. (2006) models provide the best fit to the observations, but the error bars for the points with the highest electron temperatures are large, while below 10^4 K the Izotov et al. (2006) models are virtually indistinguishable from the Garnett (1992) models.

The bottom panel of Figure 2 shows that the observed T[O II] versus T[O III] relation is in rough agreement with the Garnett (1992) prediction, although the scatter is considerably larger than in the previous two cases. This could be related to the fact that the T[O II] temperature is sensitive to the electron density through collisional de-excitation. At 10^4 K a change of 50 cm^{-3} around a nominal density of 100 cm^{-3} results in a temperature variation of ±350 K (the effect is instead negligible for the other ion temperatures, except for T[S II], for which the variation is ±260 K). Predictions of the relation between T[O II] and T[O III] from Pérez-Montero & Díaz (2003) are shown for three different values of N_e: 10, 100, and 500 cm^{-3}. The density values we derive from [S II] λ6717/[S II] λ6731 are mostly below 100 cm^{-3} (only in four cases we measure densities that are only moderately above this limit, up to 250 cm^{-3}; see Table 6), and we do not see a correlation between the measured N_e and the position of the data points in the diagram. The rms scatter of the points around the Garnett (1992) model prediction is 800 K, and does not increase with temperature, as instead suggested by the Pérez-Montero & Díaz (2003) models. Kennicutt et al. (2003) list a number of physical reasons, besides collisional de-excitation, that could help explain the scatter seen in the relation between T[O II] and T[O III], including shocks and radiative transfer effects. Observational uncertainties might play a role, too, given the large wavelength baseline between

Table 6
Measured Electron Temperatures (K) and Densities (cm^{-3})

ID (1)	T[O III] (2)	T[S III] (3)	T[N II] (4)	T[O II] (5)	T[S II] (6)	N_e (7)
1	11700 ± 500	...	...	10700 ± 900	11600 ± 1900	253
2	11900 ± 500	11800 ± 900	12600 ± 1600	11300 ± 1000	9600 ± 1000	182
3	11400 ± 900	...	...	11200 ± 1000	9400 ± 1200	20
4	10900 ± 500	11100 ± 900	...	11000 ± 900	9300 ± 1000	25
5	9200 ± 500	9000 ± 600	...	9500 ± 700	8900 ± 1200	20
6	9100 ± 500	10100 ± 800	...	9200 ± 700	11300 ± 1400	20
7	11500 ± 500	...	...	11700 ± 1200	11700 ± 1600	247
8	9400 ± 500	9900 ± 700	10200 ± 1000	9000 ± 600	7900 ± 700	20
9	8600 ± 300	8200 ± 400	...	9700 ± 700	8200 ± 700	115
10	8600 ± 300	8300 ± 400	9300 ± 600	8100 ± 500	9200 ± 1000	91
11	9500 ± 600	9300 ± 600	...	11300 ± 1000	9300 ± 1000	20
12	...	7700 ± 400	7800 ± 800	8000 ± 500	6900 ± 500	16
13	...	8800 ± 500	10500 ± 900	8200 ± 500	8400 ± 1300	14
14	8800 ± 300	8700 ± 400	8700 ± 500	10200 ± 800	7100 ± 500	57
15	...	8100 ± 400	8700 ± 800	9500 ± 700	7500 ± 600	30
16	...	8200 ± 600	9600 ± 1000	9100 ± 700	10200 ± 1100	20
17	8100 ± 300	8800 ± 500	9500 ± 600	8000 ± 500	7600 ± 600	20
18	...	8800 ± 500	8400 ± 600	10700 ± 900	6700 ± 500	20
19	8500 ± 300	8300 ± 400	9100 ± 600	8100 ± 500	9900 ± 1400	20
20	8200 ± 300	8200 ± 400	9400 ± 600	9100 ± 600	8200 ± 700	91
21	...	8000 ± 500	8400 ± 600	9300 ± 700	8600 ± 900	87
22	...	7900 ± 400	8000 ± 500	8800 ± 600	7600 ± 700	34
23	8000 ± 400	8300 ± 500	8800 ± 500	9800 ± 700	8500 ± 800	30
24	8400 ± 300	...	9200 ± 500	9800 ± 700	6400 ± 500	88
25	...	8400 ± 600	9900 ± 1000	10500 ± 900	7500 ± 700	54
26	9000 ± 400	9000 ± 500	9800 ± 600	10600 ± 800	10600 ± 1300	43
27	11100 ± 500	11300 ± 800	10900 ± 900	9800 ± 700	9400 ± 900	20
28	10500 ± 400	10300 ± 900	11800 ± 1700	10500 ± 800	8300 ± 700	20

[O II] λ3727 and the auroral line [O II] λ7325, and the contamination of the latter (which is actually [O II] λλ7320,7330) by airglow OH lines at λλ7316, 7329, and 7341 Å (wavelengths from Osterbrock et al. 1996). We note that we have corrected the auroral line intensity [O II] λ7325/Hβ for recombination into the upper level (following Liu et al. 2000), although the effect is found to be at most 6%.

We have measured the [S II] λλ4069,4076 auroral lines (abbreviated [S II] λ4072 in Table 3) for all the objects in our sample, allowing the derivation of T[S II] temperatures. In many cases, however, the measurement of these lines is made uncertain at the moderate resolution of our spectra by the presence of the nearby Hγ line, which often presents absorption wing components from the underlying stellar population. In Figure 3, which shows T[S II] as a function of T[O II], we do not observe any clear correlation. The plot agrees on average with the predictions by Pérez-Montero & Díaz (2003), shown for N_e = 10 and 100 cm^{-3}, that T[S II] < T[O II]. This result could arise from the fact that the S^+-emitting zone does not coincide with the O^+ zone, due to the lower ionization potential of S^0 (10.4 eV) relative to that of O^0 (13.6 eV). The scatter of the points in Figure 3 is very large, and also in this case we do not find that the position in the diagram corresponds to the measured value of N_e, i.e., the points at the bottom do not have systematically larger densities.

In light of the results obtained for the different ion temperatures, and in particular of the tightness of the relation between T[O III] and T[S III] and the good match with the model predictions, we have adopted a three-zone ionization representation of the H II regions in NGC 300, and, following Kennicutt et al. (2003) and Bresolin et al. (2004, 2005), we used the relations between temperatures in the different zones given by Garnett (1992)

$$T[\mathrm{S\,III}] = 0.83\,T[\mathrm{O\,III}] + 1700\ \mathrm{K}, \quad (2)$$

$$T[\mathrm{N\,II}] = T[\mathrm{O\,II}] = 0.70\,T[\mathrm{O\,III}] + 3000\ \mathrm{K}. \quad (3)$$

These scaling relations allow us to calculate the temperatures in the intermediate- and low-ionization zones, once the high-ionization zone temperature T[O III] is known. On the other hand, in the eight H II regions of our sample for which [O III] λ4363 was not detected, it is possible to derive T[O III] from the knowledge of T[S III] through Equation (2). In order to reduce the random errors when both T[O III] and T[S III] are available, we adopted for the temperature of the high-ionization zone (where the emission from O^{++} and Ne^{++} originates) the weighted average between T[O III] and the temperature derived by the inversion of Equation (2). In a similar way, for the intermediate-ionization zone (S^{++}, Ar^{++}) we calculated a weighted average of T[S III] and the temperature resulting from the scaling relation. For the low-ionization zone (O^+, N^+, S^+), we took the T[O II] value that results from the insertion of the high-ionization zone temperature derived in the previous step into Equation (3). The temperatures for the three ionization zones derived with this method are summarized in Table 7. The errors quoted reflect the 1σ uncertainties in the line fluxes used for the computation of the temperatures, and include an additional term, added in quadrature, that estimates the uncertainty in the scaling relations (±200 K for T[S III] versus T[O III], ±400 K for T[O II] versus T[O III]).

In Figure 4, we plot the radial trend of T[O III], where we have used full symbols for the H II regions for which we determined

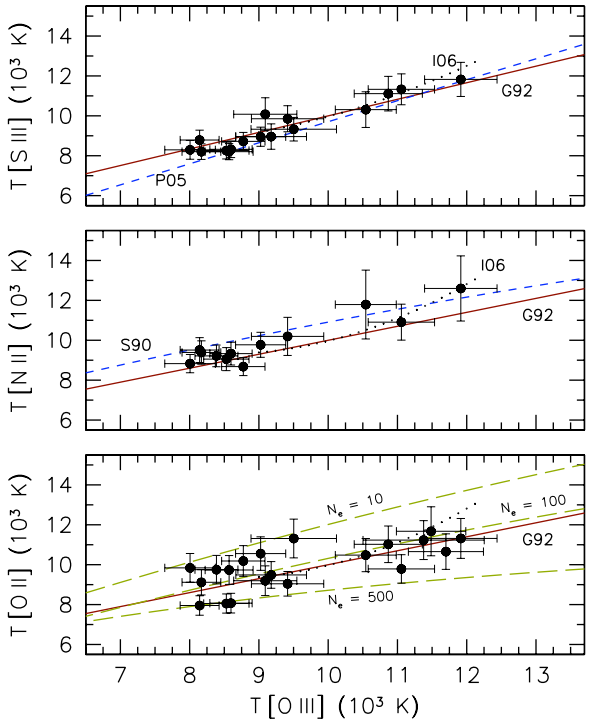

Figure 2. Relations between T[O III] and T[S III] (top), T[N II] (middle), and T[O II] (bottom). The data points are compared with the model predictions of Garnett (1992, G92: red full line), Pérez-Montero & Díaz (2005, P05: dashed blue line), the high-metallicity models of Izotov et al. (2006, I06: dotted curve), and Stasińska (1990, S90: dashed blue line). The dashed lines in the bottom panel show models from Pérez-Montero & Díaz (2003), calculated for N_e = 10, 100, and 500 cm^{-3}.

(A color version of this figure is available in the online journal.)

this temperature directly from [O III] λ4363, and open symbols for the eight H II regions for which we derived T[O III] from [S III] λ6312 and inverting Equation (2). There is a clear outlier, object No. 7 in our list (= De 30, further discussed in Sections 6.3 and 6.4), with respect to the temperature gradient defined by the remaining H II regions. After excluding this object, a weighted linear least-square fit yields

$$T[\mathrm{O\,III}] = 6920(\pm130) + 4470(\pm260)R/R_{25}, \qquad (4)$$

where the temperature is expressed in degrees K. The regression is shown with a continuous line in Figure 4. The gradient corresponds to 840 ± 50 K kpc^{-1}. This value can be compared to the results obtained for other galaxies, such as M33, where Magrini et al. (2007) measured 570 ± 130 K kpc^{-1}, and the Milky Way, for which Deharveng et al. (2000) found 372 ± 38 K kpc^{-1} from hydrogen radio recombination lines (a flatter slope, 287 ± 46 K kpc^{-1}, was obtained by Quireza et al. 2006). For M101, from Kennicutt et al. (2003) we derived 290 ± 25 K kpc^{-1}. This quick comparison suggests that smaller, less luminous spiral galaxies have steeper temperature gradients than larger ones. Since the temperature gradients are due to variations in abundances, with cooling via line emission being more effective at high metallicities, this is a reflection of the fact that more luminous spiral galaxies tend to have flatter abundance gradients when expressed in dex kpc^{-1} (Garnett et al. 1997).

4. CHEMICAL ABUNDANCES

The ionic abundances were derived with the *ionic* program in IRAF from the electron temperatures adopted in the three

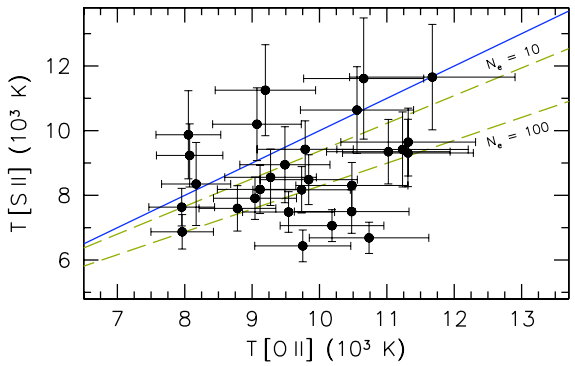

Figure 3. Relation between T[O II] and T[S II]. The dashed lines show models from Pérez-Montero & Díaz (2003), calculated for N_e = 10 and 100 cm^{-3}. The blue continuous line represents the one-to-one relation.

(A color version of this figure is available in the online journal.)

ionization zones (Table 7) and the reddening-corrected emission line fluxes in Tables 3 and 4. The results are presented in Table 8, where for each ionic species X we provide the quantity 12 + log(X/H$^+$).

In order to derive the total chemical abundances, we need to adopt an ionization correction scheme to account for unseen ionization stages of the chemical elements. The method we followed is summarized below.

Oxygen, nitrogen, and neon. For these elements, we have adopted the commonly used schemes

$$\mathrm{O/H} = \mathrm{O^+/H^+ + O^{++}/H^+}$$

justified by the absence of He II λ4686, which is emitted in high-excitation H II regions and planetary nebulae, where the O^{3+} contribution is non-negligible (Kingsburgh & Barlow 1994);

$$\mathrm{N/O} = \mathrm{N^+/O^+}$$
$$\mathrm{Ne/O} = \mathrm{Ne^{++}/O^{++}}$$

which derive from the similarity of the ionization potentials of the ions involved (Peimbert & Costero 1969).

Sulfur and argon. We have adopted the metallicity-dependent ionization correction factors (ICFs) of Izotov et al. (2006) that are based on photoionization model sequences in which the ionizing flux was calculated by means of Starburst 99 (Leitherer et al. 1999). The models that are relevant for our work are those labeled *"high Z"* [12 + log(O/H) > 8.2] and *"intermediate Z"* [7.6 < 12 + log(O/H) ⩽ 8.2] by Izotov et al. (2006), who parameterize the ICFs in terms of the observed O$^+$/O.

Figure 5 displays, as a function of O$^+$/O, the abundance ratios S/O (top), Ar/O (middle), and Ne/O (bottom) that are obtained. We use open symbols to represent H II regions without an [O III] λ4363 line detection. For these objects, the electron temperature of the high-ionization O^{++} region was therefore determined from [S III] λ6312 only, rather than a combination of this line with [O III] λ4363. In general, the abundance ratios derived for these H II regions have larger error bars, but they agree in our plots with the abundance ratios obtained from the use of [O III] λ4363. The S/O and Ar/O abundance ratios do not show any appreciable trend with the nebular excitation (a linear regression is consistent with zero slope), as expected. Ne/O displays a weak dependence on excitation, which could reflect the inadequacy of the ICF that we used. Adopting alternative schemes (e.g., Izotov et al. 2006; Pérez-Montero et al. 2007) results in a steeper dependence than seen in Figure 5. We point out, however, that some of the Ne/O data

Table 7
Adopted Electron Temperatures (K)

ID (1)	$T(O^{++}, Ne^{++})$ (2)	$T(S^{++}, Ar^{++})$ (3)	$T(O^{+}, N^{+}, S^{+})$ (4)
1	11700 ± 500	11400 ± 500	11200 ± 600
2	12000 ± 500	11600 ± 400	11400 ± 500
3	11400 ± 900	11100 ± 800	11000 ± 700
4	11000 ± 400	10800 ± 400	10700 ± 500
5	9100 ± 400	9200 ± 400	9300 ± 500
6	9300 ± 400	9400 ± 400	9500 ± 500
7	11500 ± 500	11200 ± 500	11000 ± 500
8	9500 ± 400	9600 ± 400	9700 ± 500
9	8300 ± 300	8600 ± 300	8800 ± 400
10	8400 ± 300	8600 ± 300	8900 ± 400
11	9400 ± 500	9500 ± 400	9600 ± 500
12	7200 ± 500	7700 ± 400	8000 ± 600
13	8600 ± 700	8800 ± 500	9000 ± 600
14	8700 ± 300	8900 ± 300	9100 ± 400
15	7700 ± 600	8100 ± 400	8400 ± 600
16	7900 ± 700	8200 ± 600	8500 ± 600
17	8200 ± 300	8600 ± 300	8700 ± 400
18	8600 ± 600	8800 ± 500	9000 ± 600
19	8400 ± 300	8600 ± 300	8900 ± 400
20	8100 ± 200	8400 ± 200	8700 ± 400
21	7600 ± 600	8000 ± 500	8300 ± 600
22	7500 ± 600	7900 ± 400	8300 ± 600
23	8000 ± 300	8300 ± 300	8600 ± 500
24	8400 ± 300	8700 ± 300	8900 ± 500
25	8100 ± 700	8400 ± 600	8700 ± 700
26	9000 ± 300	9100 ± 300	9300 ± 500
27	11200 ± 400	11000 ± 400	10800 ± 500
28	10500 ± 400	10400 ± 400	10400 ± 500

points have considerable error bars, and that by removing the single, high-excitation object No. 7 the significance of the excitation dependence of Ne/O is reduced considerably. The observational uncertainties and the poor knowledge of the ionization correction for Ne at low excitation prevent us to draw firm conclusions on the behavior of Ne in the H II regions of NGC 300.

The dashed horizontal lines in Figure 5 represent the solar abundance ratios published by Lodders (2003, L03). For argon, we also display the solar Ar/O ratio taken from Asplund et al. (2005, A05), to show that considerable uncertainty is still present in some of the solar abundance ratios. The weighted mean abundances of S and Ne relative to O that we find in NGC 300 (continuous lines) are in good agreement with the solar values by Lodders (2003). On the other hand, our mean Ar/O ratio is intermediate between the solar values of Lodders (2003) and Asplund et al. (2005). We note here that if we had adopted the ionization correction scheme for argon used in earlier works by our group (e.g., Bresolin et al. 2004), we would have obtained a mean Ar/O value nearly coincident with the Lodders (2003) value. The weighted means and standard deviations that we obtain in our NGC 300 sample are the following:

$$\log(\mathrm{S/O}) = -1.61 \pm 0.06\ (\odot : -1.50 \pm 0.06),$$
$$\log(\mathrm{Ar/O}) = -2.32 \pm 0.08\ (\odot : -2.14 \pm 0.09),$$
$$\log(\mathrm{Ne/O}) = -0.82 \pm 0.07\ (\odot : -0.82 \pm 0.11),$$

where the solar values in brackets are taken from Lodders (2003). Table 9 summarizes the oxygen abundances, together with the N/O, S/O, Ar/O, and Ne/O abundance ratios.

As a consistency check, we have calculated the O/H abundances by using the [O II] λ7325 line, instead of [O II] λ3727,

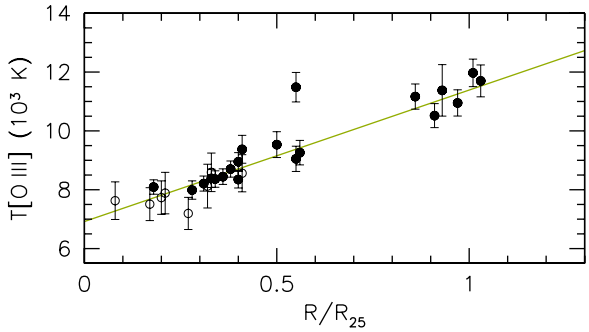

Figure 4. T[O III] radial gradient, in terms of the isophotal radius R_{25}. The linear least-square fit to the data, with the exception of the outlier (region No. 7 = De 30), is shown by the line. In this and several of the following plots, open disk symbols are used to represent the eight H II regions whose [O III] λ4363 line is not detected, and for which T_e was derived from [S III] λ6312 alone.
(A color version of this figure is available in the online journal.)

to measure the ionic abundance O^+/H^+. This provides a further test of our flux calibration and line flux measurements. We obtained a mean difference $\log(O/H)_{7325} - \log(O/H)_{3727} = 0.009 \pm 0.009$, indicating that no systematic difference exists between the two measurements. This supports the result obtained by Kniazev et al. (2004) from the spectra of more than 200 H II galaxies from the Sloan Digital Sky Survey [$\log(O/H)_{7325} - \log(O/H)_{3727} = -0.002 \pm 0.002$], and the conclusion that [O II] λ7325 can be used to measure O^+/H^+ ionic abundances, albeit with larger uncertainties, in those cases where [O II] λ3727 is unavailable (e.g., Izotov et al. 2006).

4.1. Trends with O/H

The relationships between the abundances of N, Ar, S, and Ne relative to oxygen ($\log X/O$) and the oxygen abundance $12 + \log(O/H)$ are displayed in Figure 6. The M101 comparison sample from Kennicutt et al. (2003) is shown with the square symbols. The well known increase of N/O with O/H, attributed to a secondary component in the nucleosynthesis of nitrogen (Vila Costas & Edmunds 1993), is apparent in Figure 6. The independence of the Ne/O ratio on O/H is also clear from the bottom panel of this figure. Less clear is the situation for Ar/O and S/O. In both cases, the significance of the correlation with O/H is fairly low. However, if we look at the dependence of the abundance ratios with galactocentric distance, as done in Figure 7, the correlation appears more clearly defined. The dotted lines represent the weighted linear regressions to the data points. For Ne/O, the data are clearly compatible with a constant Ne/O across the disk of the galaxy. The galactocentric dependence of N/O is consistent with the result that this abundance ratio is a function of O/H, as seen in Figure 6. The Spearman rank correlation coefficient for both S/O and Ar/O as a function of radius is 0.41, and the slopes are significant at approximately the 3σ level. These trends are opposite in sign to the one detected for S/O in M33 by Vílchez et al. (1988) and in M51 by Díaz et al. (1991). More recent studies on the chemical composition of these two galaxies, however, have failed to reproduce these results (Bresolin et al. 2004; Magrini et al. 2007).

Despite the statistical significance of the result, we are reluctant to draw conclusions on the real trend of S/O and Ar/O with oxygen abundance, with the consequent implication for the nucleosynthetic origin of S and Ar (these elements are thought to be produced by the same massive stars that produce oxygen). First of all, we stress that the ICFs for sulfur and argon

Table 8
Ionic Abundances: $12 + \log(X/H^+)$

ID	O^+	O^{++}	S^+	S^{++}	N^+	Ne^{++}	Ar^{++}
(1)	(2)	(3)	(4)	(5)	(6)	(7)	(8)
1	7.78 ± 0.09	7.85 ± 0.06	5.62 ± 0.05	6.31 ± 0.03	6.29 ± 0.05	7.10 ± 0.07	5.70 ± 0.04
2	7.58 ± 0.08	8.02 ± 0.05	5.49 ± 0.04	6.36 ± 0.03	6.03 ± 0.05	7.27 ± 0.06	5.75 ± 0.03
3	7.98 ± 0.12	7.46 ± 0.11	5.98 ± 0.07	6.21 ± 0.06	6.55 ± 0.07	6.49 ± 0.12	5.59 ± 0.06
4	7.91 ± 0.09	7.84 ± 0.06	5.81 ± 0.05	6.44 ± 0.03	6.52 ± 0.05	7.06 ± 0.07	5.85 ± 0.04
5	8.18 ± 0.11	8.08 ± 0.08	6.16 ± 0.06	6.69 ± 0.04	6.84 ± 0.07	7.24 ± 0.09	6.00 ± 0.05
6	8.11 ± 0.10	8.08 ± 0.07	6.00 ± 0.06	6.56 ± 0.04	6.78 ± 0.06	7.33 ± 0.09	5.97 ± 0.04
7	7.54 ± 0.08	8.33 ± 0.06	5.83 ± 0.05	6.58 ± 0.03	6.36 ± 0.05	7.69 ± 0.07	6.02 ± 0.04
8	8.12 ± 0.10	7.80 ± 0.07	6.04 ± 0.06	6.54 ± 0.04	6.85 ± 0.06	6.99 ± 0.09	5.90 ± 0.04
9	8.06 ± 0.11	8.23 ± 0.06	6.03 ± 0.06	6.77 ± 0.03	6.94 ± 0.07	7.47 ± 0.07	6.15 ± 0.04
10	8.06 ± 0.11	8.21 ± 0.05	5.71 ± 0.06	6.75 ± 0.03	6.70 ± 0.06	7.49 ± 0.07	6.10 ± 0.03
11	8.07 ± 0.11	7.98 ± 0.08	6.03 ± 0.06	6.62 ± 0.04	6.80 ± 0.07	7.17 ± 0.10	6.05 ± 0.05
12	8.44 ± 0.16	7.62 ± 0.16	6.47 ± 0.09	6.80 ± 0.06	7.29 ± 0.10	0.00 ± 0.00	5.93 ± 0.07
13	8.17 ± 0.14	7.89 ± 0.13	6.05 ± 0.08	6.64 ± 0.06	7.01 ± 0.09	6.92 ± 0.16	5.93 ± 0.07
14	8.16 ± 0.10	8.05 ± 0.05	6.09 ± 0.06	6.77 ± 0.03	7.01 ± 0.06	7.22 ± 0.06	6.17 ± 0.03
15	8.19 ± 0.15	7.97 ± 0.14	6.24 ± 0.08	6.84 ± 0.06	7.26 ± 0.09	6.98 ± 0.17	6.15 ± 0.07
16	8.31 ± 0.17	7.94 ± 0.17	6.26 ± 0.09	6.76 ± 0.07	7.21 ± 0.10	7.05 ± 0.20	6.10 ± 0.08
17	8.17 ± 0.11	8.18 ± 0.06	5.94 ± 0.06	6.78 ± 0.03	6.89 ± 0.07	7.25 ± 0.07	6.08 ± 0.04
18	8.19 ± 0.14	7.89 ± 0.13	6.23 ± 0.08	6.73 ± 0.06	7.08 ± 0.09	7.01 ± 0.15	6.13 ± 0.06
19	8.09 ± 0.11	8.08 ± 0.06	5.98 ± 0.06	6.70 ± 0.03	6.80 ± 0.06	7.22 ± 0.07	5.93 ± 0.04
20	8.03 ± 0.11	8.27 ± 0.05	5.83 ± 0.06	6.82 ± 0.03	6.83 ± 0.07	7.46 ± 0.07	6.19 ± 0.03
21	8.28 ± 0.17	8.04 ± 0.17	6.32 ± 0.09	6.86 ± 0.07	7.37 ± 0.10	7.12 ± 0.19	6.22 ± 0.08
22	8.39 ± 0.16	7.94 ± 0.15	6.44 ± 0.09	6.77 ± 0.06	7.31 ± 0.09	7.15 ± 0.17	6.11 ± 0.07
23	8.12 ± 0.12	8.24 ± 0.07	5.98 ± 0.07	6.75 ± 0.03	6.91 ± 0.07	7.48 ± 0.09	6.19 ± 0.04
24	8.11 ± 0.11	8.11 ± 0.06	5.99 ± 0.06	6.75 ± 0.04	6.94 ± 0.07	7.10 ± 0.08	6.09 ± 0.04
25	8.31 ± 0.17	8.04 ± 0.17	6.18 ± 0.09	6.74 ± 0.07	7.10 ± 0.10	7.08 ± 0.20	6.18 ± 0.08
26	7.92 ± 0.10	8.16 ± 0.06	5.79 ± 0.06	6.73 ± 0.03	6.68 ± 0.06	7.30 ± 0.07	6.12 ± 0.04
27	7.98 ± 0.08	7.66 ± 0.05	6.19 ± 0.05	6.35 ± 0.03	6.70 ± 0.05	6.85 ± 0.06	5.67 ± 0.03
28	8.00 ± 0.09	7.88 ± 0.06	5.89 ± 0.05	6.49 ± 0.03	6.57 ± 0.05	7.06 ± 0.07	5.82 ± 0.04

are still poorly known, and depend strongly on the ionizing properties of the stellar models used to derive them. Despite great progress in stellar atmosphere codes of massive stars in recent years, important differences in the calculated spectral energy distributions and ionizing output between models still exist (Simón-Díaz & Stasińska 2008). An increase of 15% in the ICFs at low metallicity [$12 + \log(O/H) < 8.2$] would remove the radial trends seen for S and Ar in Figure 7. However, we stress that the result does not depend on the particular choice of ICFs we made. Adopting the ICF(S) suggested by Stasińska (1978), as generalized by Barker (1980), and adopted in several recent papers (e.g., Bresolin et al. 2004; Pérez-Montero et al. 2006), or the ICF(Ar) from Pérez-Montero et al. (2007), would lead to a similar galactocentric dependence of these two elements.

Kennicutt et al. (2003) pointed out that the ionization correction scheme they adopted, based on the Stasińska (1978) formulation, is likely to underestimate the ICF for sulfur at high-excitation levels (and their correction for argon is based on the assumption that $Ar/S = Ar^{++}/S^{++}$). However, we do not detect a significant radial gradient in excitation, as measured by O^+/O. We do measure a small gradient in the ionizing stellar temperatures, by means of the radiation softness parameter $\eta = (O^+/O^{++})/(S^+/S^{++})$ (Vílchez & Pagel 1988), in the sense that hotter temperatures are found at larger radii (see Section 6.4), but the quantification of the effect is highly model dependent. It is unclear whether this could affect the magnitude of the ionization correction, but we could speculate that harder ionizing spectra, as found at large galactocentric distances, could lead to increased proportions of S^{3+} and Ar^{3+}, and therefore larger ICFs.

In alternative, observational uncertainties could be responsible for the observed trends, although we were not able to isolate a mechanism that would systematically decrease S/O and Ar/O with increasing galactocentric distance. One possibility is that the emission line fluxes in the red spectral region are depressed relative to those in the blue. However, as just mentioned, we cannot identify a reason why this effect should depend on galactocentric distance. Moreover, the fluxes of lines in the red are tied to Balmer or Paschen lines, whose intensity follows precise theoretical (case B) values.

We close this section by pointing out that, interestingly, a decreasing trend of S/O with radius has been reported in NGC 300 by Christensen et al. (1997), although the statistical significance of their result is likely to be quite small, as it rests mostly on a single H II region at small galactocentric distance. An S/O ratio that is significantly lower than the average found in the rest of the disk is also observed for an H II region in M101 located near the isophotal radius (Garnett & Kennicutt 1994). Unfortunately, sulfur and argon lines were not detected in the outermost ($R/R_{25} = 1.25$) H II region so far spectroscopically observed in M101 (Kennicutt et al. 2003), therefore we cannot confirm that a decrease in S/O exists in this galaxy.

4.2. Helium

In order to estimate the He/H abundances in the NGC 300 H II regions, we relied on the measured intensities of the two neutral helium lines, He I λ5876 and He I λ6678. No He^{++} contribution to the total helium abundance is expected, because high-excitation lines, in particular He II λ4686, are not observed

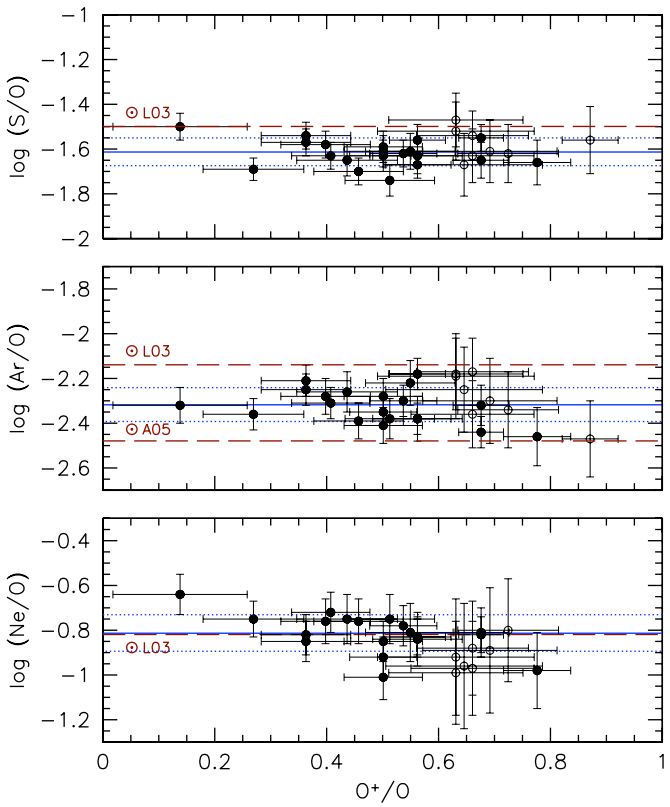

Figure 5. S/O (top), Ar/O (middle), and Ne/O (bottom) abundance ratios as a function of O^+/O. The dashed lines represent the solar abundance ratios from Lodders (2003, L03) and Asplund et al. (2005, A05). The weighted means calculated from our data points are shown by the continuous horizontal lines, while dotted lines are drawn at one standard deviation above and below the mean. The open disk symbols are used for H II regions whose [O III] λ4363 line is missing, and for which T_e was derived from [S III] λ6312 alone.

(A color version of this figure is available in the online journal.)

in our sample. We accounted for the absorption line component of the lines arising from the underlying stellar population, following the procedure outlined by Kennicutt et al. (2003), and which is based on the use of the measured equivalent widths of the emission lines. The effect for the NGC 300 sample is <5% (except for No. 22, for which it is 10%). The He^+/H^+ ionic ratios were derived from the line strengths adopting the line emissivities of Porter et al. (2007) for He I and Storey & Hummer (1995) for H I, both calculated at the O^{++} temperature derived from the auroral line analysis.

The correction for the presence of neutral helium, which can be significant at low excitation, was carried out using a method based on the radiation softness parameter η (Vílchez 1989; Izotov et al. 1994). We derived an approximate analytical relation between η and ICF(He) from the models of Stasińska et al. (2001), obtaining

$$\mathrm{ICF(He)} = 1.585 + \log\eta\,(1.642\log\eta - 1.948) \qquad (5)$$

valid in the $0.6 < \log\eta < 2.0$ interval. For $\log\eta < 0.6$ (harder spectra, or hotter ionizing stars), we took ICF(He) = 1. Multiplying the He^+/H^+ ionic ratios by ICF(He), we then obtained the total helium abundances given in Column 8 of Table 9 and displayed in Figure 8. The weighted mean He/H = 0.090 ± 0.007 is consistent with the observations in our comparison sample in M101 (square symbols). In this galaxy, Kennicutt et al. (2003) observed an increase of the He/H ratio at the high abundance end, at small galactic radii. We do not see the same effect in NGC 300. Figure 9 shows that the He/H ratio does not correlate with galactocentric distance. The different behavior between the two galaxies could be related to the smaller central metallicity in NGC 300 and the modest radial chemical composition gradient in its disk.

5. THE METALLICITY GRADIENT IN NGC 300

Since the works of Searle (1971) and Shields (1974), the radial trends of H II region chemical abundances in external spiral galaxies have been the subject of many investigations. Among these we mention the comparative studies, based on strong-line methods, of relatively large samples of galaxies by Vila-Costas & Edmunds (1992), Zaritsky et al. (1994), and Pilyugin et al. (2004), the auroral line-based studies of individual galaxies by Garnett et al. (1997) and Kennicutt et al. (2003), and the reviews by Henry & Worthey (1999) and Garnett (2004). The H II region abundance gradient in NGC 300 has been measured by several authors, including Pagel et al. (1979), Webster & Smith (1983), and Deharveng et al. (1988), and has been also re-derived from the data published by those authors by Vila-Costas & Edmunds (1992) and Zaritsky et al. (1994). However, none of these gradient determinations are based on the detection of [O III] λ4363, and were obtained from the R_{23} indicator. Following our determination of the direct abundances of 28 H II regions in Section 4, we present here the metallicity gradient in NGC 300 as obtained from the auroral line method, and compare it with the result from the young stellar content.

H II regions. For the H II regions we assume, as is customary, that the overall metallicity is well traced by the oxygen abundance. This is justified by the fact that in H II regions about half of the atoms in the gas phase heavier than hydrogen and helium are oxygen atoms (e.g., in the case of the Orion Nebula; Esteban et al. 2004). Carbon can be as abundant as oxygen at high metallicity (García-Rojas et al. 2006), but it is much more difficult to measure in the optical, as it emits only feeble recombination lines.

An important quantity that affects our comparison with the stellar metallicities is represented by the amount of oxygen that is depleted onto dust grains in ionized nebulae. The gas-phase composition of the most common ions of the diffuse interstellar matter (ISM) in the solar neighborhood is derived from weak UV absorption features measured along sight lines to various stars. For the case of oxygen, observations of O I λ1356 with the *Hubble Space Telescope* (Meyer et al. 1998; Cartledge et al. 2004) and other faint O I transitions with the *Far Ultraviolet Spectroscopic Explorer* (Oliveira et al. 2005) provide a value for the gas-phase oxygen abundance near the Sun ($d < 1$ kpc) of $12 + \log(O/H) = 8.54 \pm 0.02$. From the Galactic H II region radial abundance gradient, measured at the solar galactocentric distance, Pilyugin et al. (2006) find a good agreement with the interstellar absorption line results. For the specific case of the Orion Nebula, which, at a distance of 389 pc from the Sun (Sandstrom et al. 2007), can be taken as representative of the gas-phase composition in the solar vicinity, Esteban et al. (2004) obtained $12 + \log(O/H) = 8.51 \pm 0.03$ using the nebular collisionally excited lines, in good agreement with the results above. However, from O II recombination lines the same authors obtained an oxygen abundance higher by 0.14 dex, $12 + \log(O/H) = 8.65 \pm 0.03$, a manifestation of the abundance discrepancy observed in a number of Galactic and extragalactic H II regions (García-Rojas et al. 2007).

Quantifying the amount of oxygen that is locked up into dust grains is made difficult by the uncertainties in the total

Table 9
Total Abundances

ID (1)	R/R_{25} (2)	12 + log (O/H) (3)	log (N/O) (4)	log (S/O) (5)	log (Ar/O) (6)	log (Ne/O) (7)	He/H (8)
1	1.03	8.12 ± 0.05	−1.49 ± 0.10	−1.70 ± 0.06	−2.39 ± 0.08	−0.76 ± 0.10	0.080 ± 0.007
2	1.01	8.15 ± 0.04	−1.55 ± 0.09	−1.69 ± 0.05	−2.36 ± 0.07	−0.75 ± 0.08	0.092 ± 0.011
3	0.93	8.09 ± 0.09	−1.43 ± 0.14	−1.66 ± 0.10	−2.46 ± 0.13	−0.98 ± 0.17	0.083 ± 0.011
4	0.97	8.18 ± 0.05	−1.39 ± 0.10	−1.62 ± 0.06	−2.30 ± 0.07	−0.78 ± 0.09	0.102 ± 0.013
5	0.55	8.43 ± 0.07	−1.34 ± 0.13	−1.63 ± 0.08	−2.38 ± 0.10	−0.84 ± 0.12	0.086 ± 0.011
6	0.56	8.40 ± 0.06	−1.33 ± 0.12	−1.74 ± 0.07	−2.38 ± 0.09	−0.75 ± 0.11	0.092 ± 0.012
7	0.55	8.40 ± 0.05	−1.18 ± 0.10	−1.50 ± 0.06	−2.32 ± 0.08	−0.64 ± 0.09	0.083 ± 0.009
8	0.50	8.29 ± 0.07	−1.27 ± 0.12	−1.65 ± 0.08	−2.32 ± 0.09	−0.81 ± 0.11	0.085 ± 0.011
9	0.40	8.46 ± 0.06	−1.12 ± 0.13	−1.58 ± 0.06	−2.28 ± 0.08	−0.76 ± 0.10	0.092 ± 0.011
10	0.36	8.45 ± 0.05	−1.36 ± 0.12	−1.63 ± 0.06	−2.31 ± 0.07	−0.72 ± 0.09	0.079 ± 0.010
11	0.41	8.33 ± 0.07	−1.27 ± 0.13	−1.61 ± 0.08	−2.22 ± 0.10	−0.81 ± 0.13	0.089 ± 0.011
12	0.27	8.50 ± 0.14	−1.15 ± 0.19	−1.56 ± 0.15	−2.47 ± 0.17	...	0.060 ± 0.007
13	0.33	8.35 ± 0.11	−1.15 ± 0.17	−1.63 ± 0.12	−2.36 ± 0.15	−0.97 ± 0.21	0.083 ± 0.010
14	0.38	8.41 ± 0.06	−1.15 ± 0.12	−1.56 ± 0.07	−2.18 ± 0.07	−0.83 ± 0.08	0.091 ± 0.011
15	0.20	8.39 ± 0.11	−0.93 ± 0.18	−1.47 ± 0.12	−2.18 ± 0.16	−0.99 ± 0.23	0.088 ± 0.011
16	0.21	8.47 ± 0.13	−1.10 ± 0.20	−1.61 ± 0.14	−2.30 ± 0.19	−0.89 ± 0.28	0.079 ± 0.010
17	0.31	8.47 ± 0.06	−1.28 ± 0.13	−1.63 ± 0.07	−2.35 ± 0.07	−0.92 ± 0.09	0.091 ± 0.011
18	0.41	8.37 ± 0.10	−1.11 ± 0.17	−1.54 ± 0.11	−2.17 ± 0.15	−0.88 ± 0.21	0.090 ± 0.011
19	0.34	8.39 ± 0.06	−1.30 ± 0.13	−1.61 ± 0.07	−2.41 ± 0.08	−0.85 ± 0.09	0.103 ± 0.013
20	0.18	8.47 ± 0.05	−1.20 ± 0.13	−1.57 ± 0.06	−2.25 ± 0.07	−0.82 ± 0.09	0.091 ± 0.011
21	0.08	8.48 ± 0.12	−0.92 ± 0.19	−1.52 ± 0.13	−2.19 ± 0.19	−0.92 ± 0.26	0.075 ± 0.010
22	0.17	8.53 ± 0.12	−1.09 ± 0.18	−1.62 ± 0.13	−2.34 ± 0.17	−0.80 ± 0.23	0.077 ± 0.009
23	0.28	8.48 ± 0.06	−1.21 ± 0.14	−1.65 ± 0.07	−2.26 ± 0.09	−0.75 ± 0.11	0.085 ± 0.010
24	0.33	8.41 ± 0.06	−1.17 ± 0.13	−1.59 ± 0.07	−2.28 ± 0.08	−1.01 ± 0.10	0.082 ± 0.010
25	0.32	8.50 ± 0.13	−1.22 ± 0.20	−1.67 ± 0.14	−2.25 ± 0.19	−0.96 ± 0.28	0.081 ± 0.010
26	0.40	8.36 ± 0.05	−1.25 ± 0.12	−1.54 ± 0.06	−2.21 ± 0.07	−0.85 ± 0.09	0.092 ± 0.011
27	0.86	8.15 ± 0.06	−1.29 ± 0.10	−1.55 ± 0.06	−2.44 ± 0.07	−0.82 ± 0.08	0.084 ± 0.010
28	0.91	8.25 ± 0.06	−1.43 ± 0.10	−1.67 ± 0.06	−2.38 ± 0.07	−0.83 ± 0.09	0.102 ± 0.012

(gas phase + dust) amount that is assumed, and usually taken from the composition of the Sun, B stars, or young cool stars (Sofia 2004). The study of the Orion Nebula and its surroundings provides one way of estimating the amount of O depletion, from the comparison of the ionized gas with young B stars. The mean O abundance from the investigation of three B0.5 V stars in the Trapezium cluster by Simón-Díaz et al. (2006) is 12 + log(O/H) = 8.63 ± 0.03. Taking the composition of the diffuse clouds in the solar neighborhood and the collisionally excited line result for the Orion Nebula from Esteban et al. (2004) would suggest a depletion factor of approximately −0.1 dex. Recently, Przybilla et al. (2008) measured the chemical composition of six early-B stars (luminosity classes III–IV) in the solar neighborhood (d < 500 pc), obtaining 12 + log(O/H) = 8.76 ± 0.03, which, compared with the diffuse ISM abundance, would imply an oxygen dust depletion of approximately −0.2 dex. Mesa-Delgado et al. (2009) also estimated a −0.2 dex depletion factor in the Orion Nebula for the case in which temperature fluctuations in the ionized gas are neglected.

For our comparison in NGC 300, we will adopt −0.1 dex as the minimum depletion value that is required to match stellar and gaseous oxygen abundances in the solar vicinity, with the understanding that it could be as high as −0.2 dex, and assuming that the result, obtained for our immediate surroundings in the Milky Way can be generalized to external galaxies. Furthermore, the caveat remains that the study of recombination lines in H II regions yield larger abundances (about 0.2 dex) than collisionally excited lines.

Blue supergiants. A catalog of nearly 70 early-type supergiant stars in NGC 300 was compiled by Bresolin et al. (2002a), based on VLT multi-object spectroscopy, with the goal of providing high-quality stellar spectra for chemical abundance follow-up studies. As a proof of concept, these authors analyzed the metallicities of one B9-A0 Ia star and one A0 Ia star. Later, Urbaneja et al. (2005b) derived abundances of several elements (C, N, O, Mg, Si) in six early-B (B0.5–B3) supergiants, spatially distributed along a wide range of galactocentric distances, allowing them to carry out a first comparison with the oxygen abundance gradient derived from H II regions. The oxygen gradient derived from the six stars was −0.060 ± 0.049 dex kpc^{-1} (scaled to our adopted distance to the galaxy), with a central abundance of 12 + log(O/H) = 8.58 ± 0.13. However, due to the lack of direct measurements of electron temperatures for the NGC 300 H II regions, the nebular abundances were estimated from the application of several calibrations of the R_{23} strong-line abundance indicator to the emission line fluxes compiled by Deharveng et al. (1988). Significantly different nebular abundance gradients were obtained by varying the adopted R_{23} calibration, both in terms of slope and zero point, making it difficult to reach meaningful conclusions regarding the comparison between the stellar and nebular galactocentric abundance trends.

More recently, Kudritzki et al. (2008) analyzed a sample of 24 A-type supergiants (spectral types from B8 to A4) drawn from the Bresolin et al. (2002a) catalog, deriving stellar parameters and metallicities using a grid of line-blanketed stellar models and NLTE line formation calculations. While in this case the authors did not derive abundances of individual elements, because at the low resolution of the VLT spectra the features in A supergiant spectra are mostly blends of iron, titanium, chromium, and other lines, the fitting of features across the whole wavelength range covered was found to be quite sensitive

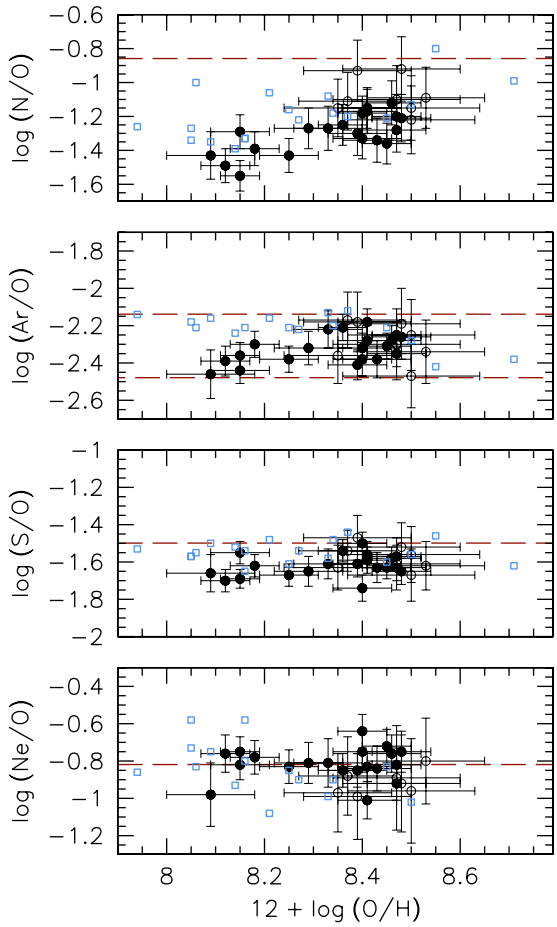

Figure 6. Trends of N/O, Ar/O, S/O, and Ne/O with oxygen abundance. In each plot, we also include as a comparison sample the M101 data from Kennicutt et al. (2003, squares). The horizontal dashed lines are the solar values shown in Figure 5. The open disk symbols are used for H II regions whose [O III] λ4363 line is missing.

(A color version of this figure is available in the online journal.)

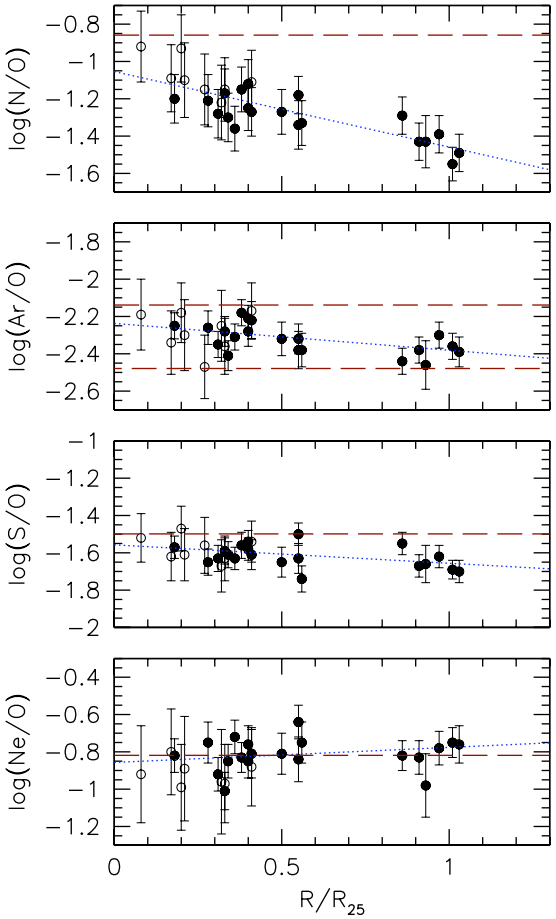

Figure 7. Observed trends of the abundance ratios N/O, Ar/O, S/O, and Ne/O with galactocentric distance, in units of the isophotal radius R_{25}. The horizontal dashed lines represent the solar values, as in Figure 5. The dotted lines show the weighted linear regressions to the observations. As in previous figures, open symbols are used for H II regions whose [O III] λ4363 line is missing.

(A color version of this figure is available in the online journal.)

to the choice of the model metallicities (the typical estimated uncertainty was 0.2 dex). In the construction of the models, the solar abundance pattern of the various chemical elements was assumed, from Grevesse & Sauval (1998). The metallicities of the A supergiants obtained by Kudritzki et al. (2008) refer therefore to the abundances of a variety of heavy elements (Mg, Si, S, Ti, Cr, Fe) combined, whose individual abundance ratios reflect the solar abundance pattern. While this restriction can be relaxed in future modeling, allowing, for example, the investigation of variations of the α/Fe element ratio in galaxies, the metallicity values obtained in the case of the NGC 300 A supergiants should be regarded as representative of the overall metal content in the stellar atmospheres of these young stars.

In comparing the metallicities from the supergiants stars with the oxygen abundances from the H II regions, we make the assumption that for the A stars oxygen scales with metallicity, and that the solar metallicity value corresponds to $12 + \log(\mathrm{O/H})_{\odot} = 8.66$ (Asplund et al. 2005). Figure 10 shows the radial metallicity gradient determined from the H II regions (circles) and blue supergiants (star symbols: B supergiants; open squares: A supergiants; galactocentric distances for the stars have been recomputed adopting the galaxy parameters in Table 1). For clarity, the error bars for the stellar data are omitted, but typical uncertainties are on the order of 0.2 dex. As a reference, we include in the plot the mean level of the nebular oxygen

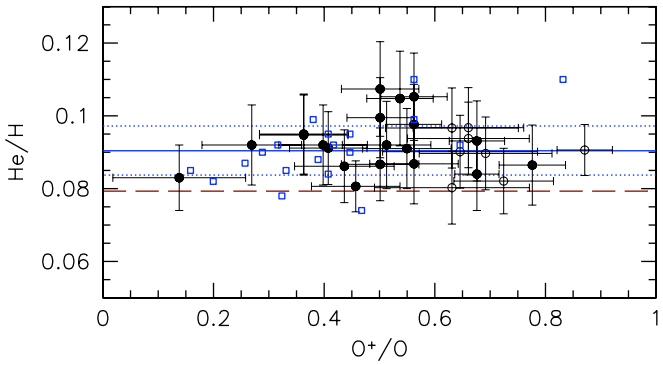

Figure 8. He/H abundance ratio as a function of excitation O^+/O. The horizontal dashed line represents the solar value from Lodders (2003). The weighted mean is shown by the continuous horizontal line, with dotted lines drawn at one standard deviation above and below the mean. The M101 sample of Kennicutt et al. (2003) is shown with open square symbols.

(A color version of this figure is available in the online journal.)

abundances measured in the Magellanic Clouds by Russell & Dopita (1990), as well as the solar value from Asplund et al. (2005). In the figure, we have omitted the outlier A supergiant A10 from Kudritzki et al. (2008). As in previous figures, we use open circles for H II regions that have no

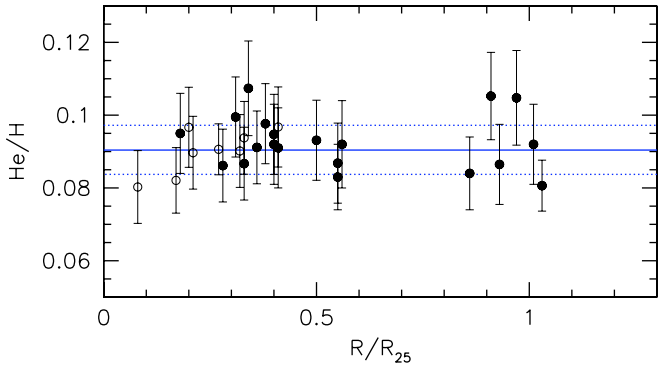

Figure 9. He/H abundance ratio as a function of galactocentric distance. The weighted mean is shown by the continuous horizontal line, with dotted lines drawn at one standard deviation above and below the mean.

(A color version of this figure is available in the online journal.)

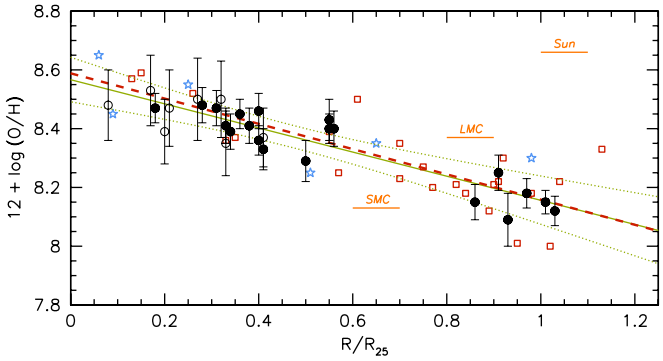

Figure 10. Radial metallicity gradient obtained from H II regions (circles) and blue supergiants (star symbols: B supergiants; open squares: A supergiants). The weighted regression line to the H II region data is shown by the continuous (green) line. The dotted lines show the 95% confidence level interval for the regression line. The dashed line represents the weighted regression to the BA supergiant star data. For reference, we include the oxygen abundances of the Magellanic Clouds and the solar photosphere.

(A color version of this figure is available in the online journal.)

[O III] λ4363 detection, and therefore the electron temperature in their O^{++}-emitting region was derived from [S III] λ6312. The corresponding oxygen abundances have larger errors than those for the H II regions for which we have used both [O III] λ4363 and [S III] λ6312 to obtain T_e.

A weighted linear regression to the H II region data, with weights equal to the reciprocal of the variance, yields

$$12 + \log(\mathrm{O/H})_{\mathrm{gas}} = 8.57(\pm0.02) - 0.41(\pm0.03)R/R_{25} \quad (6)$$

and is shown with a continuous line in Figure 10. The weighted regression to the combined A and B supergiant data, using the variances from Kudritzki et al. (2008) and Urbaneja et al. (2005b), is

$$12 + \log(\mathrm{O/H})_{\mathrm{stars}} = 8.59(\pm0.05) - 0.43(\pm0.06)R/R_{25} \quad (7)$$

and is shown with a dashed line in Figure 10. A straightforward error analysis shows that the slopes and the intercepts of the two regressions are not significantly different. The virtual coincidence of the slopes of the nebular and stellar abundance gradients is remarkable. This result is quite robust, since it does not depend on the somewhat uncertain dust depletion factor, which affects the absolute abundance values, and the possible effects of temperature fluctuations on the derived abundances, because they appear to be independent of metallicity. From the H II region regression, which has the smaller errors, we derive an oxygen abundance gradient of -0.077 ± 0.006 dex kpc^{-1}, while the blue supergiants yield -0.081 ± 0.011 dex kpc^{-1} (the small difference relative to the value published by Kudritzki et al. 2008, -0.083 dex kpc^{-1}, is due to the slightly different orientation parameters used to calculate the galactocentric distances).

The intercepts of the linear fits are virtually coincident. Due to our initial assumption that the A supergiant oxygen abundances scale with the metallicity obtained from the analysis of the line blends in their spectra, the vertical positions of the A supergiant data in Figure 10 depend on the choice of the solar oxygen abundance, whereas the H II region abundances do not. However, in Figure 10 we do not detect a significant offset between the A supergiants and the B supergiants, which provide direct measurements (albeit model dependent) of the oxygen abundance via the stellar O II spectral features. In any case, it is important to remember that additional effects, such as the uncertainties of the atomic parameters on the derived abundance, also influence the comparison of the absolute values of the chemical abundances. For example, the default atomic data used by IRAF's *nebular* tasks distributed with STSDAS Version 3.8 (2008 February), which had not been updated since 1997, would yield a mean O/H value lower by about 0.04 dex than reported here.

The agreement we find between nebular and stellar abundances leaves little room for effects that would systematically increase the nebular abundances, such as metal depletion onto dust grains, or large-scale temperature fluctuations. By considering the modest dust depletion factor of −0.1 dex for oxygen discussed earlier the intercept of the linear regression to the H II region data for O/H would still be consistent with the A supergiant fit, within the 1σ uncertainties. We estimate that the stellar and nebular intercepts would differ at the 95% confidence level once we reach $12 + \log(\mathrm{O/H})_{\mathrm{gas}} = 8.70$ (neglecting other sources of systematic errors, such as uncertainties in the atomic parameters and the solar metallicity). This would leave no room for temperature fluctuation effects. Clearly, measurements of metal recombination lines in this galaxy would be helpful to secure constraints on the abundance discrepancy factor in NGC 300.

We do not see any evidence in Figure 10 for a break in the abundance gradient of NGC 300, in particular for a steepening of the gradient in the inner disk, which was suggested by Vila-Costas & Edmunds (1992), who applied the R_{23} index on a compilation of published data to derive chemical abundances. This result was not confirmed by Zaritsky et al. (1994), who could not exclude that some of the breaks in the line ratios observed for a few galaxies at certain galactocentric distances might not represent actual bends in the abundance gradients (as more recently concluded by Pilyugin 2003). A central steepening might be present in other galaxies, for example, M33 (Vílchez et al. 1988; Magrini et al. 2007), but a simple exponential function appears to be sufficient to describe the dependence of O/H on radius in NGC 300. Zaritsky et al. (1994) defined the "characteristic" oxygen abundance of a galaxy as the value measured at $0.4\,R_{25}$. This quantity correlates with the integrated galaxy metallicity (Moustakas & Kennicutt 2006). From Equation (6), we find a characteristic abundance $12 + \log(\mathrm{O/H}) = 8.41 \pm 0.04$ for NGC 300.

The distribution of the H II region data points in Figure 10 has quite a small dispersion, with an rms residual from the linear fit of only 0.05 dex, which is similar to the measurement

uncertainty of the most accurate O/H abundances presented in Table 9 (the reduced χ^2 statistics equals 1.2, implying that the abundance error estimates are realistic). The scatter is smaller than what has been observed from auroral line measurements in other galaxies, such as M101 (Kennicutt et al. 2003; 0.09 dex, comparable to the measurement errors), and especially M33, where Rosolowsky & Simon (2008) found a dispersion which is considerably larger than the measurement errors, with an intrinsic variance of 0.11 dex (from their data, the rms scatter computed in the same way as in the case of NGC 300 is 0.16 dex). In NGC 300, the observed oxygen abundance scatter at a given radius is therefore consistent with the measurement errors. This suggests that azimuthal abundance variations are negligible at the level of precision attained in this work. However, the number of H II regions observed should be increased considerably, especially in the outer disk, in order to test for azimuthal variations.

6. DISCUSSION

6.1. Comparisons between Gas and Stars in Other Galaxies

In this section, we briefly summarize the main results regarding the comparison of chemical abundances obtained from H II regions and blue supergiants in nearby galaxies, in order to put our result for NGC 300 into a wider context. We limit our comparisons to the abundances of oxygen, since this is, in most cases, the only chemical element that can be reliably measured in both gas and stars (nitrogen is subject to evolutionary effects, i.e., enrichments and depletions, in early-type stars). We also do not strive for an exhaustive review of the subject, and concentrate only on H II regions as representative of the gaseous abundances, since in NGC 300 planetary nebulae abundances have not been published yet (but a companion paper, by M. Peña et al. 2009, is in preparation).

Some of the previous comparisons in external galaxies have suffered from the lack of direct abundances (those based on T_e determinations) of H II regions, and had therefore to deal with the systematic uncertainties introduced by the use of different strong-line abundance indicators. This was the case in the previous study of six B supergiants in NGC 300 by Urbaneja et al. (2005b), or in the analysis of B, A, and F supergiants in M31 (Smartt et al. 2001; Trundle et al. 2002; Venn et al. 2000). Firmer results have been obtained in nearby dwarf galaxies, in which the low oxygen abundances favor, due to the higher electron temperature resulting from smaller gas cooling, the detection of T_e-sensitive auroral lines, in particular [O III] λ4363. In most cases, a very good agreement is found between the oxygen abundance from B-type stars and H II regions (Magellanic Clouds: Trundle & Lennon 2005; Hunter et al. 2007—WLM and IC 1613: Bresolin et al. 2006, 2007; Urbaneja et al. 2008—NGC 6822: Lee et al. 2006—NGC3109: Evans et al. 2007; Peña et al. 2007). However, the metallicity in these small, chemically homogeneous systems is low, typically below the Small Magellanic Cloud (SMC) value $12 + \log(\mathrm{O/H}) = 8.1$ (1/4 solar).

The comparison at higher metallicities becomes more challenging, as explained above, due to the difficulty of measuring reliable H II region chemical abundances as the nebular cooling efficiency increases (by contrast, stellar features become more pronounced). Metallicities that are larger than those encountered in dwarf galaxies can be found in the central regions of spirals (obviously we are not considering ellipticals), but the number of target galaxies that are suitable for a comparison with the stellar studies is quite limited. In fact, prior to our work in NGC 300, comparisons have been carried out only in the Milky Way and in M33 (todate no direct nebular abundances are available in M31). In both cases, the picture is not as clear as one would hope. In the Milky Way, where both H II regions and B stars can be traced in the optical preferentially at galactocentric distances larger than about 6 kpc, due to dust obscuration in the direction of the Galactic center, B-type main-sequence stars have been found to define a radial oxygen abundance gradient of -0.067 ± 0.008 dex kpc^{-1} (Rolleston et al. 2000; see also Smartt & Rolleston 1997; Gummersbach et al. 1998) that well matches the gradient obtained for H II regions by various authors, including Shaver et al. (1983) and Afflerbach et al. (1997). On the other hand, more recent studies of H II regions (Deharveng et al. 2000) and B stars (Daflon & Cunha 2004) find significantly flatter slopes for the oxygen gradient, -0.039 ± 0.005 and -0.031 ± 0.012 dex kpc^{-1}, respectively, i.e., about a factor of 2 smaller. These works underline the need for accurate nebular electron temperatures and for a self-consistent NLTE analysis of homogeneous samples of OB stars, in order to improve chemical abundance determinations in these young populations. Comparisons in single, nearby star-forming regions appear particularly important in assessing the reliability of the analysis methods. A recent example is given by Simón-Díaz et al. (2006) who, using the latest generation of hot star models, have found a remarkable agreement in the oxygen surface content of three Trapezium cluster B main-sequence stars [average $12 + \log(\mathrm{O/H}) = 8.63 \pm 0.03$] and of the gas-phase abundance of the Orion Nebula [$12 + \log(\mathrm{O/H}) = 8.65 \pm 0.03$], analyzed from high-resolution spectroscopy by Esteban et al. (2004).

Comparative studies of H II region and hot star abundances in M33 started with McCarthy et al. (1995) and Monteverde et al. (1996), who established with the first metallicity determinations for A and B supergiants in this galaxy a rough agreement with the nebular abundances. The more recent quantitative B supergiant work by Urbaneja et al. (2005a) derived a linear radial oxygen abundance gradient of -0.06 ± 0.02 dex kpc^{-1}, which is in agreement with the H II region O/H gradient of -0.054 ± 0.011 dex kpc^{-1} measured across the whole optical disk of the galaxy by Magrini et al. (2007). The latter authors, following Vílchez et al. (1988) and Urbaneja et al. (2005a), proposed that the combined nebular + stellar gradient could be better represented by a steeper portion in the inner ($R <$ 3 kpc) disk relative to the outer part of the galaxy. However, the picture is complicated by additional H II region studies, reporting slopes of the O/H gradient that are both steeper (-0.12 ± 0.02 dex kpc^{-1}: Vílchez et al. 1988) and shallower (-0.012 ± 0.011 dex kpc^{-1}: Crockett et al. 2006; $-0.027 \pm$ 0.011 dex kpc^{-1}: Rosolowsky & Simon 2008). These last authors suggest that the different determinations can, in fact, be compatible with each other, because the errors in the slopes are likely to be underestimated in the case of a large intrinsic scatter of the abundances around the mean gradient. We add that the blue supergiants studied by Urbaneja et al. (2005a) provide ∼0.3 dex systematically larger abundances than the H II regions studied by Magrini et al. (2007).

In conclusion, there is a still rather small body of evidence that in general metallicity determinations carried out by means of H II regions and hot stars (B dwarfs and supergiants, and A supergiants) in galaxies are in rough agreement, but some apparently significant differences are borne out when looking at the details. The specific cases of the abundance gradient in the two best-studied spiral galaxies, the Milky Way and M33, reveal

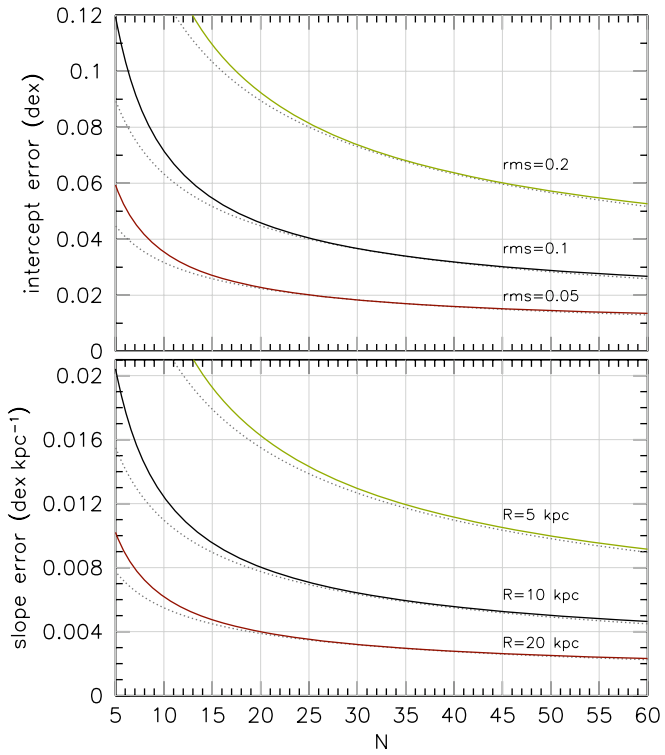

Figure 11. Results of Monte Carlo simulations of the errors measured in the intercept (top) and the slope (bottom) of exponential fits to the abundance distribution of H II regions uniformly distributed in radius within a spiral galaxy as a function of the number of data points. Curves for the intercept error are drawn for three different values of the rms scatter (0.05, 0.1, and 0.2 dex). The curves in the bottom panel are drawn for a single rms scatter of 0.1 dex, and three different sizes of the galaxy (5, 10, and 20 kpc). The analytical results of Dutil & Roy (2001) are shown by the dotted lines.

(A color version of this figure is available in the online journal.)

unacceptable inconsistencies between H II region abundances from different authors, that are hard to explain simply in terms of measurement errors. A critical aspect of the nebular work is represented by the accuracy of the electron temperatures, which are usually derived from optical auroral lines (hydrogen radio recombination lines can also be used in the Milky Way; Shaver et al. 1983). This problem can be partially circumvented by deriving abundances from mid-IR (e.g., [Ne II] λ12.8 μm, [Ne III] λ15.6 μm, [S III] λ18.7 μm, [S IV] λ10.5 μm) and far-IR lines (e.g., [O III] λλ52,88 μm), which are insensitive to T_e. This method has been pursued with success in the Milky Way (Martín-Hernández et al. 2002; Rudolph et al. 2006), but has been rarely applied to derive abundance gradients for external spiral galaxies. A recent example is the study of S and Ne abundances in M33 by Rubin et al. (2008), carried out with the *Spitzer Space Telescope* (unfortunately, the oxygen lines lie outside of the spectroscopic range covered by *Spitzer*).

Sample size can also be an issue in deriving reliable H II region abundance gradients, especially if the intrinsic abundance scatter is large (as suggested by Rosolowsky & Simon 2008 for the case of M33). Dutil & Roy (2001) estimated that a minimum of 16 H II regions is required in order to obtain zero points with an accuracy of ±0.05 dex or better when the rms scatter is 0.1 dex. We have run a series of Monte Carlo simulations to independently estimate the errors in both the intercept and the slope of a single exponential fit to data points distributed uniformly in galactocentric radii, for different values of the scatter and the size of the galaxy. We essentially confirm the results of Dutil & Roy (2001), except that as the number N of objects considered becomes smaller our simulations predict progressively larger errors (see Figure 11). The top panel of Figure 11 shows that for an intrinsic rms abundance scatter of 0.05 dex (as appears to be the case of NGC 300, as shown here, and the Milky Way; Deharveng et al. 2000) 10 H II regions are sufficient to determine the intercept of the fit to better than 0.04 dex, but the required N rises quickly, with the square of the intrinsic rms scatter. The curves in the bottom panel for the slope error as a function of N were drawn for a constant rms scatter of 0.1 dex, and different galactic radii (5, 10, and 20 kpc). The slope error at a given N is the same for a given ratio between these two quantities. Measuring at the 3σ level a shallow abundance gradient (0.02–0.03 dex kpc^{-1}) could require more than 30 H II regions, as in the case of a galaxy with a radius of 10 kpc and a scatter of 0.1 dex (black curve).

6.2. Strong-line Abundances

Comparisons of strong-line abundance determination methods for H II regions have already been carried out by several authors, and we refer the reader to the rather vast recent literature on the subject (Kennicutt et al. 2003; Pérez-Montero & Díaz 2005; Nagao et al. 2006; Yin et al. 2007; Liang et al. 2007; Shi et al. 2007; Kewley & Ellison 2008). In the specific case of NGC 300, Urbaneja et al. (2005b) have already shown how the adoption of three popular calibrations of the R_{23} method affects the nebular abundances in relation to the B supergiant oxygen abundances. We can also look at the abundance gradients determined by various authors. As an example, using their R_{23} calibration, Zaritsky et al. (1994) obtained a slope of $-0.61 \pm 0.05\ {R_{25}}^{-1}$, about 50% larger than our value, and an extrapolated central abundance $12 + \log(\mathrm{O/H})_o = 8.97$, compared to our value of 8.57. Deharveng et al. (1988), with the Dopita & Evans (1986) R_{23} calibration, obtained virtually the same values (slope: −0.63, intercept: 8.95). Vila-Costas & Edmunds (1992), with yet another R_{23} calibration, obtained a slope of $-0.49\ {R_{25}}^{-1}$ and an intercept $12 + \log(\mathrm{O/H})_o = 8.78$ (using their one-component fit rather than the two-part gradient). As made clear by a few empirical studies (Kennicutt et al. 2003; Bresolin et al. 2004), the direct abundances obtained from the T_e-sensitive auroral lines provide values in the metal-rich, upper branch of R_{23} that are considerably lower than previous R_{23} calibrations. The effect appears to be more significant at high metallicity, so that the slopes derived from the direct method are shallower. In fact, the gradient derived by Pilyugin et al. (2004) from the published data using the P-method, which is empirically tied to [O III] λ4363 abundances in other galaxies, is in good agreement with our direct measurements (slope: −0.40, intercept: 8.49).

We can now illustrate how different strong-line methods compare to the T_e-based direct method, as applied to the H II regions in NGC 300. For simplicity, we limit our choice to only three methods: (1) $R_{23} = ([\mathrm{O\,II}]\,\lambda3727 + [\mathrm{O\,III}]\,\lambda\lambda4959,5007)/\mathrm{H}\beta$, with the popular theoretical calibrations by McGaugh (1991; using the analytical forms provided by Kuzio de Naray et al. 2004), and Tremonti et al. (2004; the analytical fit in their Equation (1)), (2) the theoretical prediction for the [N II] λ6583/[O II] λ3727 indicator by Kewley & Dopita (2002), and (3) $\mathrm{N2} = \log([\mathrm{N\,II}]\,\lambda6583/\mathrm{H}\alpha)$, empirically calibrated by Pettini & Pagel (2004). The output abundances of these methods and their relative calibrations span the abundance range typically covered by strong-line indicators. Figure 12 shows the abundances that result from the application of these different

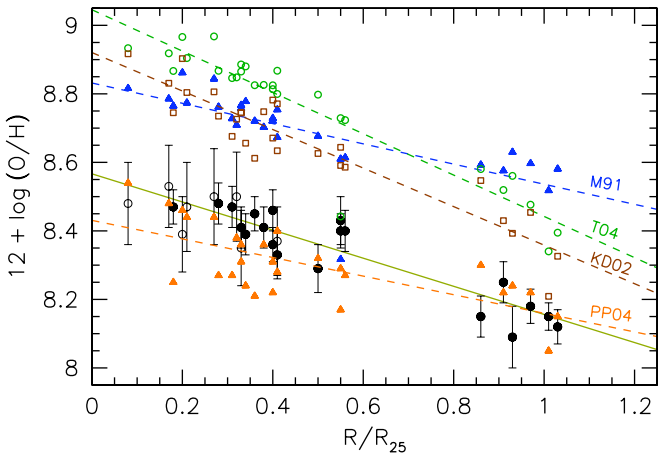

Figure 12. Galactocentric distribution of the abundance values obtained from different strong-line methods and calibrations: R_{23} (McGaugh 1991: M91, blue triangles; Tremonti et al. 2004: T04, green circles), [N II]/[O II] (Kewley & Dopita 2002: KD02, open squares), and N2 (Pettini & Pagel 2004: PP04, orange triangles). Linear least-squares fits are shown by the dashed lines, and labeled with the appropriate reference. The direct abundances determined from our work are shown by the full and open circle symbols, and the corresponding linear fit is shown by the continuous line (same as in Figure 10).

(A color version of this figure is available in the online journal.)

indicators and calibrations, together with the direct abundances derived in Section 4, as a function of galactocentric distance of the H II regions. For each method, we include the linear least-square fit to the data.

Figure 12 illustrates the well known result that calibrations of strong-line indices based on theoretical modeling can provide abundance estimates that are larger, by several tenths of a dex, than those from empirical calibrations (Bresolin et al. 2004). The better agreement between our direct abundance gradient and the gradient obtained from N2, calibrated by Pettini & Pagel (2004), is no surprise, since this calibration is directly tied to [O III] λ4363 measurements in extragalactic H II regions. For R_{23}, we have assumed that all H II regions, including those at large galactocentric distance, belong to the upper branch of the calibration, even if their [N II]/Hα, the usual discriminator between lower and upper branches, is around the turnover value (around [N II]/Hα = −1.1 to −1.3; Kewley & Ellison 2008). Adopting the lower branch calibration would move the outer data points down by ∼0.4 dex, bringing them close to the empirical results, but producing a much steeper gradient or an abundance jump from the inner half of the disk. A plot of O/H versus R_{23} (not shown) suggests that the assumption that all objects belong to the upper branch is justified.

The H II region No. 7 (= De 30) in our list (Table 1) is a clear outlier in relation to the abundance gradient measured with the R_{23} method, as it lies 0.35 dex below the corresponding regression line. This object is characterized by a very hard spectrum, with [O III]/[O II] = 9.1, that makes it stand out also in the traditional BPT (Baldwin et al. 1981) diagnostic diagrams. This is likely related to its W–R star content (see Section 6.3). The measured log R_{23} = 1.13 is larger than the maximum value considered by the McGaugh (1991) models, and this is the likely explanation for the failure of the analytical expression used to derive O/H from R_{23}. This object's oxygen abundance does not appear to be peculiar when measured from the high signal-to-noise ratio (S/N) detection of [O III] λ4363, or from either N2 or [N II]/[O II].

Figure 12 also illustrates the fact that the slope of the radial abundance gradient can be significantly different from the one estimated from the electron temperature method. For example, the slope determined from [N II]/[O II] is −0.56 ± 0.04 dex R_{25}^{-1}, compared to −0.41 ± 0.03 dex R_{25}^{-1} from the direct method. In conclusion, we confirm earlier findings that the direct method yields oxygen abundances that are considerably smaller than some popular calibrations of strong-line methods obtained via grids of theoretical models. While the origin of the discrepancy remains unclear, the direct method result is rather robust, and is backed by the study of blue supergiants. This has obvious consequences for the study of metallicity gradients in galaxies, as exemplified in Figure 12, as well as for the derivation of chemical abundances in star-forming galaxies at high redshift.

6.3. Wolf–Rayet Stars

The detection of W–R stars in extragalactic H II regions is quite common. The broad lines emitted in the extended atmospheres of these hot, evolved massive stars are easily discerned even at relatively low S/N in the spectra of the ionized nebulae that harbor them. The first detection of W–R features in NGC 300 was carried out by D'Odorico et al. (1983), who found the characteristic "blue bump" around 4650 Å in two H II regions (our No. 5 and No. 19). Additional W–R stars have been reported by Deharveng et al. (1988), Schild & Testor (1991, 1992), Breysacher et al. (1997), Bresolin et al. (2002b), and Schild et al. (2003), whose census includes 60 known or candidate W–R stars, 21 of which have spectroscopic confirmation. As Schild et al. (2003) pointed out, 12 of the spectroscopically confirmed W–R stars are of type WC, and they estimated that the overall N(WC)/N(WN) number ratio is $\geqslant$ 1/3. This puts NGC 300 approximately in the expected location in the empirical N(WC)/N(WN) versus O/H diagram, even though, as a consequence of our improved results for the metallicity in this galaxy, the abundance value adopted for the central region by Crowther (2007) should be revised downward by approximately 0.1–0.15 dex to 12 + log(O/H) = 8.5 (the value adopted by Schild et al. 2003 was instead 12 + log(O/H) = 8.8).

We have detected W–R star features in 10 H II regions of our sample, mostly the 4650 Å bump (composed of He II λ4686 and N III λ4634–41 and/or N V λ4603–20), but also C IV λ5808 (No. 5 = De 24) and C III λ5996 (No. 19 = De 77). Our spectrum of No. 7 (= De 30, already briefly discussed in Section 6.2) also contains broad He II λλ5200, 4541, and 5411 from the embedded W–R star. This object is absent from the list of Schild et al. (2003), but corresponds to star 8 of Schild & Testor (1992), who classified it as an early WN. We confirm this classification, based on the strong He II λ4686, and the presence of N V λ4603–20. For the He II λ4686 line of this star, we measure a luminosity of 3.8 × 10^{35} erg s^{-1} (for D = 1.88 Mpc), an equivalent width of 175 Å and an FWHM of 35 Å. With these measurements, we find very good agreement with the properties of WN3–4 stars in the LMC (of comparable metallicity) presented by Crowther & Hadfield (2006).

We summarize in Table 10 the W–R star detections in our H II region sample, providing spectral types and references from previous work. We report a new detection in No. 12 (= De 45), and assign a WNL classification, based on the presence of N III λ4634–41, of comparable strength to He II λ4686, and the absence of N V λ4603–20 in emission. We also uncovered the blue bump feature in No. 14, which corresponds to De 53A in Deharveng et al. (1988), while Schild et al. (2003) report W–R stars in the nearby regions De 53B and De 53C.

Table 10
W–R Star Detections

ID	Type	Reference	Comment
(1)	(2)	(3)	(4)
5	WC	D 2	
7	WNE	ST 8	
12	WNL		New detection
14	WC4, WN	S 2-4	In nearby regions De 53B-C
17		S 7-8	
19	WC+WN	S 11-12	
20		S 18	
23		S 35-37	
24		S 36	
26	WN7	S 49-50-51	

Notes. Column 1: H II region identification (from Table 2); Column 2: W–R classification (when available); Column 3: source of W–R data. S: Schild et al. 2003, only this reference is provided when available; D: D'Odorico et al. 1983; ST: Schild & Testor 1992; Column 4: De, Deharveng et al. 1988.

6.4. Ionizing Radiation

As mentioned earlier, the $\eta = (O^+/O^{++})/(S^+/S^{++})$ parameter introduced by Vílchez & Pagel (1988) is a measure of the softness of the ionizing radiation, its value decreasing with increasingly harder stellar ionizing continua ($\log \eta \sim 1/T_{\rm eff}$ in the blackbody case). Figure 13 (top) shows a mild radial gradient of η in NGC 300, as derived from our ionic abundances. The outlier with a much higher value of $\log \eta \simeq 0$ than the rest of the sample is our target No. 7 (= De 30), which was identified in Section 6.3 as a high-excitation H II region hosting a WNL star. This object appears as a high-surface brightness nebula, with a compact, round morphology in our Hα images.

To illustrate the behavior of η in a wider context, we have plotted in Figure 13 (bottom) a O^+/O^{++} versus S^+/S^{++}diagram that includes the NGC 300 data, as well as other H II region samples analyzed by our group, for which the ionic abundances were derived by means of auroral lines: M101 (Kennicutt et al. 2003; blue squares), M51 (Bresolin et al. 2004; orange squares), and additional galaxies from Bresolin et al. (2005, green triangles). In this diagram, objects whose nebular spectra can be characterized by similar values of the "effective" temperature of the ionizing radiation field lie along lines of constant η, as empirically verified by spatially resolved spectroscopy of nearby H II regions (Vílchez & Pagel 1988; Kennicutt et al. 2000). We have drawn two such lines for $\log \eta = 0$ and $\log \eta = 0.7$ for illustration purposes. Along lines of constant η the ionization parameter U, a measure of the ratio of ionizing photon density to the density of atoms, increases toward smaller S^+/S^{++} values (Mathis 1985).

It can be seen from Figure 13 that the majority of the H II galaxies cluster around the $\log \eta = 0.7$ line, with a dispersion that is partly due to metallicity. The region NGC 300-7 is one of a few with very hard ionizing spectra. Among these we find NGC 5471-B (identified in Figure 13), NGC 5471-A and NGC 5471-D (located in proximity of NGC 300-7 in the plot), and M51-P203 (orange square near NGC 5471-B). The unusually high temperature of the ionizing stars in NGC 5471 was already noted by Mathis (1982). Even harder spectra ($\log \eta$ between -0.2 and $+0.35$) can be found among H II galaxies (Hägele et al. 2006, 2008), which are more extreme examples of star-forming regions.

We have searched for a correlation between the hardness of the radiation, as measured by η, and the presence of W–R star

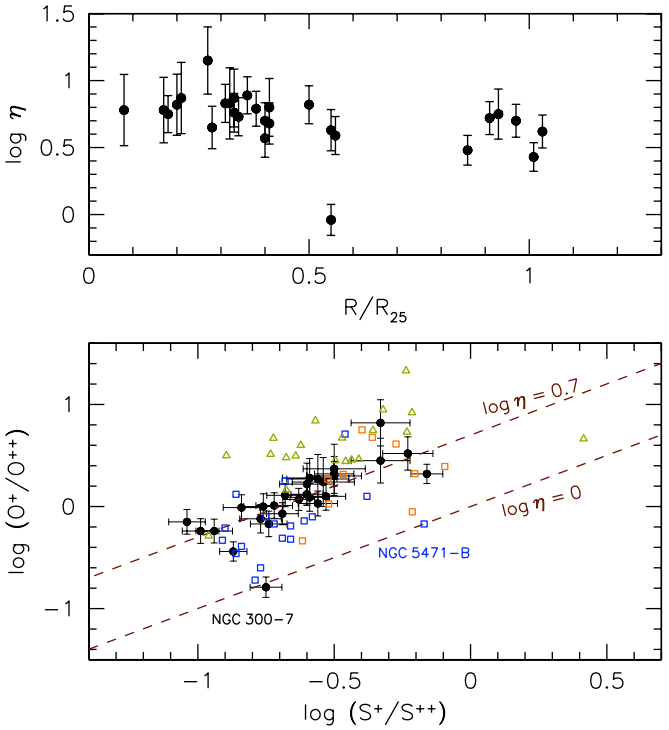

Figure 13. Top: radial gradient of $\log \eta = \log (O^+/O^{++})/(S^+/S^{++})$ in NGC 300. The outlier at $\log \eta \simeq 0$ is object No. 7. Bottom: O^+/O^{++} vs. S^+/S^{++}diagram for various H II region samples: NGC 300 (dots with error bars), M101 (blue open squares), M51 (orange open squares), and additional galaxies taken from Bresolin et al. (2005, green open triangles). In all cases, the ionic abundances were derived from the measurement of auroral lines. Two lines of constant η have been drawn at $\log \eta = 0$ and $\log \eta = 0.7$. We identify two of the H II regions discussed in the text, NGC 300-7 and NGC 5471 in M101.

(A color version of this figure is available in the online journal.)

features in the nebular spectrum. However, many of the softer spectra (high η) belong to H II regions containing W–R stars, mostly of types WC and WNL. The harder spectra could be related to the presence of high-ionization WNE stars (as found in NGC 300-7), but although we detect C III λ5696 and He II λ4686 in M51-P203 (which has one of the hardest spectra among the objects included in Figure 13), we do not find evidence for N V lines. Besides, broad W–R features are not detected in the various components of NGC 5471 in M101, although nebular He II λ4686 is present (Schaerer et al. 1999, and confirmed by our independent analysis of the spectra presented by Kennicutt et al. 2003), which is indicative of high-excitation conditions. However, high excitation is the norm among low-metallicity H II regions, as is the case of NGC 5471. Still, we think that there is circumstantial evidence to suggest that the hard spectrum of NGC 300-7 is related to the presence of an early WN star among its ionizing sources. Kennicutt et al. (2000) measured the quantity η', defined by $\log \eta' = \log \eta - 0.14/t - 0.16$ (Vílchez & Pagel 1988), which depends mildly on the electron temperature ($t = T_e/10^4$), in four H II Galactic regions ionized by W–R stars of type WN3-5, and found values between -0.2 and 0.1 (with the lower values for the earlier WN subtype). With an electron temperature around $T_e = 10^4$ K, we would then obtain $\log \eta \simeq 0.1$–0.3. This simple example illustrates the fact that the hardness of the nebular spectrum produced by a single ionizing early-type WN star is comparable to what we observe in NGC 300-7 ($\log \eta = -0.03$).

Part of the scatter of the data points in Figure 13 relative to a line of constant η is related to a metallicity trend. This

is evident in Figure 14 (top), which shows how $\log \eta$ varies with oxygen abundance for the same sample of H II regions considered in Figure 13. Excluding NGC 300-7 and M51-P203, the data points follow a linear trend defined by the following least-square fit

$$\log \eta = 1.10(\pm 0.14)x - 8.45(\pm 1.15), \quad (8)$$

where $x = 12 + \log(\mathrm{O/H})$. This result could, in principle, be affected by the dependence of η on the ionization parameter, which is known to vary with metallicity in galaxies (Dopita & Evans 1986; Bresolin et al. 1999; Dopita et al. 2006). We have investigated the effect of the ionization parameter by dividing the H II region sample into two equal-sized subsamples, of "high" and "low" U, using the fact that the S^+/S^{++} ratio, together with its more commonly used observational equivalent [S II]/[S III], is a good indicator of this nebular parameter (Díaz et al. 1991). The result is shown in Figure 14 (bottom), where the two samples are drawn with different symbols. The histogram at the bottom (drawn on an arbitrary vertical scale) indicates that the distributions of objects in each subsample in terms of O/H are only mildly skewed, with low-U H II regions favoring high abundances, and high-U H II regions favoring low abundances. The effect confirms qualitatively the finding that the ionization parameter is a decreasing function of metallicity. What is interesting, however, is that in the metallicity range covered by our data the two subsamples have a similar behavior when we consider the dependence of η on O/H. The observed trend does not appear to be generated by the ionization parameter varying systematically with metallicity, as the two subsamples have approximately the same extent in both O/H and $\log \eta$. If the η dependence on U were important, we would expect a strong dichotomy in the diagram, with high-U regions occupying only the low-η part of the plot.

The detection of a metallicity trend in the hardness of the ionizing radiation confirms earlier findings by other authors, including Vílchez & Pagel (1988) and Bresolin et al. (1999), but using a larger, homogeneous sample of extragalactic H II regions extending over nearly 0.9 dex in O/H, fully based on T_e-based abundances. The η method is successful in ranking stellar temperatures, but the quantification of the observed hardness in terms of an effective temperature of the ionizing sources is model dependent (Mathis 1985). Assigning $T_{\rm eff}$ values to the η scale would require photoionization modeling of H II regions adopting the most recent generation of stellar atmosphere models for hot stars, but this is outside of the scope of the present paper. We simply note that, while in some of the older work on the η parameter changes in the stellar initial mass function were invoked to explain the softer ionizing field at high metallicity, for example, requiring upper mass cutoffs decreasing with metallicity, the current spectral modeling of hot stars at various metallicities provides a natural explanation of the nebular observations. Softer ionizing stellar continua with increasing metallicity are theoretically expected for hot stars, due to the enhanced metal line blocking (Kudritzki 2002; Mokiem et al. 2004). Massey et al. (2004, 2005), comparing spectra of O stars located in the Milky Way and the Magellanic Clouds, and analyzed with NLTE, line-blanketed model atmospheres, find that early O stars in the SMC are 3000–4000 K hotter than their counterparts in the Milky Way. Population synthesis models that include line-blanketed atmospheres for O stars and an improved treatment of the ionizing output of W–R stars are able to reproduce the empirical radiation softening (Smith et al. 2002).

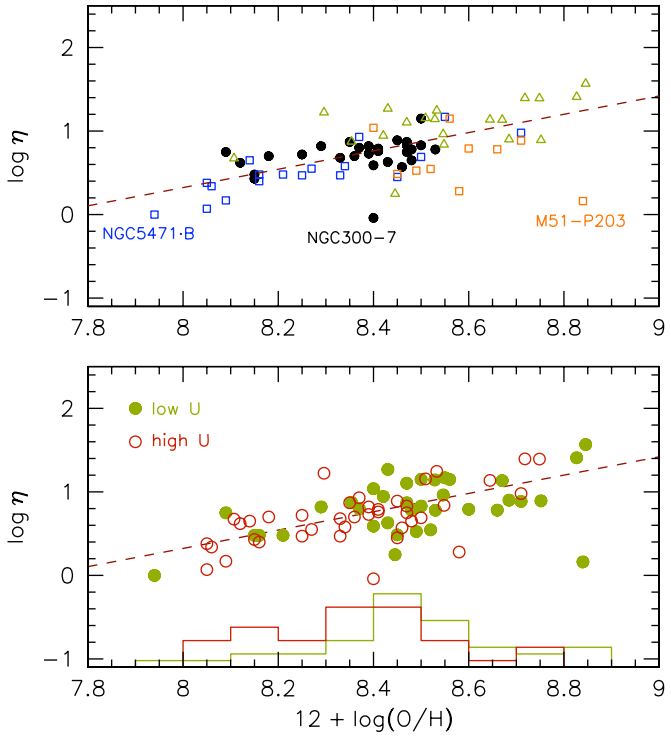

Figure 14. Top: the dependence of $\log \eta$ on O/H for the same sample of H II regions shown in Figure 13. We identify NGC 5471 in M101, NGC 300-7, and M51-P203 as three objects with particularly hard ionizing spectra. The least-square fit to the data points, excluding NGC 300-7 and M51-P203, is shown by the dashed line. Bottom: same diagram as above, using different symbols to separate H II regions with low- and high-ionization parameter U, adopting the median S^+/S^{++} ionic ratio as the cutoff value. The histograms at the bottom, drawn at an arbitrary scale, display the distribution of the two subsamples in terms of O/H.

(A color version of this figure is available in the online journal.)

7. CONCLUSIONS AND SUMMARY

The analysis of the emission lines in H II region spectra has provided the bulk of present-day abundance measurements in nearby galaxies, and is being frequently used to study the chemical composition of high-redshift star-forming galaxies. The collection of nebular data is therefore essential to infer the cosmic evolution of metallicity (Savaglio et al. 2005; Maiolino et al. 2008; Lara-López et al. 2009), although studies of the stellar metallicity as a function of redshift start to offer an alternative (Panter et al. 2008).

In the local universe, the knowledge of abundance gradients in spiral galaxies and their evolution with time provides the necessary observational constraints to the parameters that drive models of the chemical evolution of galaxies, such as the radial dependence of accretion and star formation rate in galactic disks (Matteucci & Francois 1989; Boissier & Prantzos 1999; Chiappini et al. 2001; Colavitti et al. 2008). Excluding the Milky Way and a very few nearby galaxies, such as the Magellanic Clouds, where the metal content of the young stellar populations has been derived from alternative tracers, including Cepheid variables (Luck et al. 2003; Romaniello et al. 2008) and B stars (Rolleston et al. 2000; Trundle et al. 2007), H II regions often represent the only source of present-day abundance information for star-forming galaxies.

As explained in Section 1, nebular abundances are still subject to systematic uncertainties. In the vast majority of cases, extragalactic nebular abundances are derived from strong-line

metallicity indices, due to the difficulty of detecting the faint T_e-sensitive auroral lines, such as [O III] λ4363. As discussed by several authors, large differences (up to 0.7 dex) can arise in the derived values, depending on the calibration adopted (Kewley & Ellison 2008). Empirical calibrations that are tied to auroral line measurements (such as those by Pettini & Pagel 2004; Pilyugin & Thuan 2005; Liang et al. 2007) provide considerably smaller abundance values (0.2–0.6 dex) than theoretical calibrations, which are generated from grids of photoionization models (McGaugh 1991; Kewley & Dopita 2002; Tremonti et al. 2004). This effect has been strongly manifested after the first direct measurements of electron temperatures in high-metallicity H II regions (Castellanos et al. 2002; Kennicutt et al. 2003; Bresolin et al. 2004; Bresolin 2007). The existence of temperature fluctuations within nebulae, which could be responsible for the discrepancy between nebular abundances obtained from collisionally excited lines and recombination lines, can, in principle, help to bridge the gap between direct abundances and theoretical ones. However, the importance of temperature fluctuations in explaining the abundance discrepancies in H II regions is still a controversial topic (Stasińska et al. 2007; Mesa-Delgado et al. 2008). In light of the importance of H II region abundances in disparate fields, such as the distance scale (Bono et al. 2008) and the study of gamma-ray burst progenitors (Modjaz et al. 2008), it is essential to establish the accuracy of the methods used in measuring metallicities.

Motivated by these considerations, we have obtained new H II region spectra in NGC 300. In this spiral galaxy, about 30 blue supergiants have been analyzed by our group, providing estimates of their metal content, and thus offering the possibility of a comparison between stellar and nebular abundances. What makes such a comparison more significant than previous ones is the fact that, instead of having to rely on chemical abundances obtained from strong-line methods (which are subject to the uncertainties mentioned above), we presented a sample of 28 H II regions for which we detected auroral lines ([O III] λ4363, [S III] λ6312, [N II] λ5755) used to derive electron temperatures and O, S, N, Ar, and Ne abundances. This procedure is generally considered to provide reliable abundances at least up to the solar metallicity, even though, for the reasons exposed above, it is important to test the results against other methods. The main conclusion from our work is that our stellar and nebular abundances agree very well, in the range spanned by our objects, 12 + log(O/H) approximately between 8.1 and 8.5, i.e., from the metallicity of the SMC to an intermediate value between that of the LMC and the Sun. The central abundance of NGC 300, obtained from a linear extrapolation of the H II region data, is subsolar, $12 + \log(\mathrm{O/H}) = 8.57 \pm 0.02$, and the slope of the radial abundance gradient is -0.077 ± 0.006 dex kpc^{-1}. The metallicities of the B and A supergiants analyzed by Urbaneja et al. (2005a) and Kudritzki et al. (2008) are fully consistent with the nebular results. This result leads to our main conclusion, that, in the metallicity range sampled, *direct, T_e-based chemical abundances in extragalactic H II regions are reliable measures of the nebular abundances*.

The excellent agreement that we find between nebular and stellar abundances does not exclude effects that would systematically increase the nebular abundances, such as metal depletion onto dust grains, or temperature fluctuations. However, their combined effect should be less than about 0.13 dex to be compatible with the stellar data. On the other hand, our stellar abundances do not agree with the case where the H II region abundances are derived from theoretically calibrated strong-line methods. We showed examples where the latter provide abundances that are larger than the stellar ones by 0.3 dex or more in the central galactic region. The fact that in the case of the Orion Nebula the stellar abundances are in good agreement with the gas abundances derived from metal recombination lines does not imply that a fundamental difference between extragalactic and Galactic H II regions exists, as far as metallicity determinations are concerned. It stresses the need for further comparative studies of stellar and nebular chemical compositions in the Milky Way and in other nearby spiral galaxies, including both collisionally excited lines and metal recombination lines. It is also worth pointing out that this kind of comparison is somewhat limited by systematic uncertainties, such as those related to the atomic parameters used to derive the chemical compositions.

We have briefly discussed the detection of W–R star features in our H II region spectra, and found that in one of the nebulae hosting W–R stars the ionizing field has a particularly hard spectrum, as gauged by the η parameter. We suggest that this is due to the presence of an early WN star. We have also considered a larger sample of extragalactic H II regions where T_e-based abundances are available from our previous work, and confirm previous findings about a metallicity dependence of η, in the sense that softer nebular spectra are found at higher metallicity.

F.B. gratefully acknowledges the support from the National Science Foundation grant AST-0707911. G.P. and W.G. acknowledge financial support from the Chilean Center for Astrophysics FONDAP 15010003. W.G. also acknowledges support from the BASAL Centro de Astrofisica y Tecnologias Afines for this work. We thank Grazyna Stasinska for her comments on the manuscript.

Facilities: VLT:Antu (FORS2)

REFERENCES

Afflerbach, A., Churchwell, E., & Werner, M. W. 1997, ApJ, 478, 190
Aggarwal, K. M., & Keenan, F. P. 1999, ApJS, 123, 311
Asplund, M., Grevesse, N., & Sauval, A. J. 2005, in ASP Conf. Ser. 336, Cosmic Abundances as Records of Stellar Evolution and Nucleosynthesis, ed. T. G. Barnes, III & F. N. Bash (San Francisco, CA: ASP), 25
Baldwin, J. A., Phillips, M. M., & Terlevich, R. 1981, PASP, 93, 5
Barker, T. 1980, ApJ, 240, 99
Blair, W. P., & Long, K. S. 1997, ApJS, 108, 261
Bland-Hawthorn, J., Vlajić, M., Freeman, K. C., & Draine, B. T. 2005, ApJ, 629, 239
Boissier, S., & Prantzos, N. 1999, MNRAS, 307, 857
Bono, G., Caputo, F., Fiorentino, G., Marconi, M., & Musella, I. 2008, ApJ, 684, 102
Bresolin, F. 2007, ApJ, 656, 186
Bresolin, F. 2008, in The Metal-Rich Universe, Cambridge Contemporary Astrophysics Series, ed. G. Israelian & G. Meynet (Cambridge: Cambridge Univ. Press), 155
Bresolin, F., Garnett, D. R., & Kennicutt, R. C. 2004, ApJ, 615, 228
Bresolin, F., Gieren, W., Kudritzki, R.-P., Pietrzyński, G., & Przybilla, N. 2002a, ApJ, 567, 277
Bresolin, F., Kennicutt, R. C., Jr., & Garnett, D. R. 1999, ApJ, 510, 104
Bresolin, F., Kudritzki, R.-P., Mendez, R. H., & Przybilla, N. 2001, ApJ, 548, L159
Bresolin, F., Kudritzki, R.-P., Najarro, F., Gieren, W., & Pietrzyński, G. 2002b, ApJ, 577, L107
Bresolin, F., Pietrzyński, G., Urbaneja, M. A., Gieren, W., Kudritzki, R.-P., & Venn, K. A. 2006, ApJ, 648, 1007
Bresolin, F., Schaerer, D., González Delgado, R. M., & Stasińska, G. 2005, A&A, 441, 981
Bresolin, F., Urbaneja, M. A., Gieren, W., Pietrzyński, G., & Kudritzki, R.-P. 2007, ApJ, 671, 2028
Breysacher, J., Azzopardi, M., Testor, G., & Muratorio, G. 1997, A&A, 326, 976

Butler, D. J., Martínez-Delgado, D., & Brandner, W. 2004, AJ, 127, 1472
Campbell, A., Terlevich, R., & Melnick, J. 1986, MNRAS, 223, 811
Carpano, S., Wilms, J., Schirmer, M., & Kendziorra, E. 2005, A&A, 443, 103
Cartledge, S. I. B., Lauroesch, J. T., Meyer, D. M., & Sofia, U. J. 2004, ApJ, 613, 1037
Castellanos, M., Díaz, A. I., & Terlevich, E. 2002, MNRAS, 329, 315
Chiappini, C., Matteucci, F., & Romano, D. 2001, ApJ, 554, 1044
Christensen, T., Petersen, L., & Gammelgaard, P. 1997, A&A, 322, 41
Colavitti, E., Cescutti, G., Matteucci, F., & Murante, G. 2008, A&A, 496, 429
Cowie, L. L., & Barger, A. J. 2008, ApJ, 686, 72
Crockett, N. R., Garnett, D. R., Massey, P., & Jacoby, G. 2006, ApJ, 637, 741
Crowther, P. A. 2007, ARA&A, 45, 177
Crowther, P. A., & Hadfield, L. J. 2006, A&A, 449, 711
Daflon, S., & Cunha, K. 2004, ApJ, 617, 1115
Davidge, T. J. 1998, ApJ, 497, 650
De Robertis, M. M., Dufour, R. J., & Hunt, R. W. 1987, J. R. Astron. Soc. Can., 81, 195
de Vaucouleurs, G., de Vaucouleurs, A., Corwin, H. G., Jr., Buta, R. J., Paturel, G., & Fouque, P. 1991, Third Reference Catalogue of Bright Galaxies, Vols. 1–3 (Springer: Berlin)
Deharveng, L., Caplan, J., Lequeux, J., Azzopardi, M., Breysacher, J., Tarenghi, M., & Westerlund, B. 1988, A&AS, 73, 407
Deharveng, L., Peña, M., Caplan, J., & Costero, R. 2000, MNRAS, 311, 329
Díaz, A. I., Terlevich, E., Vílchez, J. M., Pagel, B. E. J., & Edmunds, M. G. 1991, MNRAS, 253, 245
D'Odorico, S., Rosa, M., & Wampler, E. J. 1983, A&AS, 53, 97
Dopita, M. A., & Evans, I. N. 1986, ApJ, 307, 431
Dopita, M. A., et al. 2006, ApJ, 647, 244
Dutil, Y., & Roy, J.-R. 2001, AJ, 122, 1644
Edmunds, M. G., & Pagel, B. E. J. 1984, MNRAS, 211, 507
Erb, D. K., Shapley, A. E., Pettini, M., Steidel, C. C., Reddy, N. A., & Adelberger, K. L. 2006, ApJ, 644, 813
Esteban, C., Bresolin, F., Peimbert, M., García-Rojas, J., Peimbert, A., & Mesa-Delgado, A. 2009, ApJ, in press (arXiv:0905.2532)
Esteban, C., Peimbert, M., García-Rojas, J., Ruiz, M. T., Peimbert, A., & Rodríguez, M. 2004, MNRAS, 355, 229
Esteban, C., Peimbert, M., Torres-Peimbert, S., & Rodríguez, M. 2002, ApJ, 581, 241
Evans, C. J., Bresolin, F., Urbaneja, M. A., Pietrzyński, G., Gieren, W., & Kudritzki, R.-P. 2007, ApJ, 659, 1198
Froese Fischer, C., & Tachiev, G. 2004, At. Data Nucl. Data Tables, 87, 1
Froese Fischer, C., Tachiev, G., & Irimia, A. 2006, At. Data Nucl. Data Tables, 92, 607
Galavis, M. E., Mendoza, C., & Zeippen, C. J. 1995, A&AS, 111, 347
García-Rojas, J., & Esteban, C. 2007, ApJ, 670, 457
García-Rojas, J., Esteban, C., Peimbert, M., Costado, M. T., Rodríguez, M., Peimbert, A., & Ruiz, M. T. 2006, MNRAS, 368, 253
García-Rojas, J., Esteban, C., Peimbert, A., Rodríguez, M., Peimbert, M., & Ruiz, M. T. 2007, RevMexAA, 43, 3
Garnett, D. R. 1992, AJ, 103, 1330
Garnett, D. R. 2004, in Cosmochemistry: The Melting Pot of the Elements, Cambridge Contemporary Astrophysics Series, XIII Canary Islands Winter School of Astrophysics, ed. C. Esteban et al. (Cambridge: Cambridge: Univ. Press), 171
Garnett, D. R., & Kennicutt, R. C., Jr. 1994, ApJ, 426, 123
Garnett, D. R., Kennicutt, R. C., Jr., & Bresolin, F. 2004, ApJ, 607, L21
Garnett, D. R., Shields, G. A., Skillman, E. D., Sagan, S. P., & Dufour, R. J. 1997, ApJ, 489, 63
Gieren, W., Pietrzyński, G., Soszyński, I., Bresolin, F., Kudritzki, R.-P., Minniti, D., & Storm, J. 2005, ApJ, 628, 695
González-Delgado, R. M., et al. 1994, ApJ, 437, 239
Grevesse, N., & Sauval, A. J. 1998, Space Sci. Rev., 85, 161
Gummersbach, C. A., Kaufer, A., Schaefer, D. R., Szeifert, T., & Wolf, B. 1998, A&A, 338, 881
Hägele, G. F., Díaz, Á. I., Terlevich, E., Terlevich, R., Pérez-Montero, E., & Cardaci, M. V. 2008, MNRAS, 383, 209
Hägele, G. F., Pérez-Montero, E., Díaz, Á. I., Terlevich, E., & Terlevich, R. 2006, MNRAS, 372, 293
Halliday, C., et al. 2008, A&A, 479, 417
Helou, G., et al. 2004, ApJS, 154, 253
Henry, R. B. C., & Worthey, G. 1999, PASP, 111, 919
Hillier, D. J., & Miller, D. L. 1998, ApJ, 496, 407
Hudson, C. E., & Bell, K. L. 2005, A&A, 430, 725
Hummer, D. G., & Storey, P. J. 1987, MNRAS, 224, 801
Hunter, I., et al. 2007, A&A, 466, 277
Izotov, Y. I., Stasińska, G., Meynet, G., Guseva, N. G., & Thuan, T. X. 2006, A&A, 448, 955
Izotov, Y. I., Thuan, T. X., & Lipovetsky, V. A. 1994, ApJ, 435, 647
Kaufman, V., & Sugar, J. 1986, J. Phys. Chem. Ref. Data, 15, 321
Kennicutt, R. C., Bresolin, F., & Garnett, D. R. 2003, ApJ, 591, 801
Kennicutt, R. C., Bresolin, F., Jr., French, H., & Martin, P. 2000, ApJ, 537, 589
Kewley, L. J., & Dopita, M. A. 2002, ApJS, 142, 35
Kewley, L. J., & Ellison, S. L. 2008, ApJ, 681, 1183
Kingsburgh, R. L., & Barlow, M. J. 1994, MNRAS, 271, 257
Kniazev, A. Y., Pustilnik, S. A., Grebel, E. K., Lee, H., & Pramskij, A. G. 2004, ApJS, 153, 429
Kobulnicky, H. A., & Kewley, L. J. 2004, ApJ, 617, 240
Kudritzki, R. P. 2002, ApJ, 577, 389
Kudritzki, R.-P., Urbaneja, M. A., Bresolin, F., Przybilla, N., Gieren, W., & Pietrzyński, G. 2008, ApJ, 681, 269
Kuzio de Naray, R., McGaugh, S. S., & de Blok, W. J. G. 2004, MNRAS, 355, 887
Lara-López, M. A., Cepa, J., Bongiovanni, A., Castañeda, H., Pérez García, A. M., Fernández Lorenzo, M., Póvic, M., & Sánchez-Portal, M. 2009, A&A, 493, L5
Larsen, S. S., Origlia, L., Brodie, J. P., & Gallagher, J. S. 2006, MNRAS, 368, L10
Larsen, S. S., Origlia, L., Brodie, J., & Gallagher, J. S. 2008, MNRAS, 383, 263
Lee, H., Skillman, E. D., & Venn, K. A. 2006, ApJ, 642, 813
Leitherer, C., et al. 1999, ApJS, 123, 3
Lequeux, J., Peimbert, M., Rayo, J. F., Serrano, A., & Torres-Peimbert, S. 1979, A&A, 80, 155
Liang, Y. C., Hammer, F., Yin, S. Y., Flores, H., Rodrigues, M., & Yang, Y. B. 2007, A&A, 473, 411
Liu, X., Shapley, A. E., Coil, A. L., Brinchmann, J., & Ma, C.-P. 2008, ApJ, 678, 758
Liu, X.-W., Storey, P. J., Barlow, M. J., Danziger, I. J., Cohen, M., & Bryce, M. 2000, MNRAS, 312, 585
Lodders, K. 2003, ApJ, 591, 1220
Luck, R. E., Gieren, W. P., Andrievsky, S. M., Kovtyukh, V. V., Fouqué, P., Pont, F., & Kienzle, F. 2003, A&A, 401, 939
Maeder, A., & Meynet, G. 2000, ARA&A, 38, 143
Magrini, L., Vílchez, J. M., Mampaso, A., Corradi, R. L. M., & Leisy, P. 2007, A&A, 470, 865
Maier, C., Lilly, S. J., Carollo, C. M., Meisenheimer, K., Hippelein, H., & Stockton, A. 2006, ApJ, 639, 858
Maiolino, R., et al. 2008, A&A, 488, 463
Martín-Hernández, N. L., et al. 2002, A&A, 381, 606
Massey, P., Bresolin, F., Kudritzki, R. P., Puls, J., & Pauldrach, A. W. A. 2004, ApJ, 608, 1001
Massey, P., Puls, J., Pauldrach, A. W. A., Bresolin, F., Kudritzki, R. P., & Simon, T. 2005, ApJ, 627, 477
Mathis, J. S. 1982, ApJ, 261, 195
Mathis, J. S. 1985, ApJ, 291, 247
Matteucci, F., & Francois, P. 1989, MNRAS, 239, 885
McCarthy, J. K., Lennon, D. J., Venn, K. A., Kudritzki, R.-P., Puls, J., & Najarro, F. 1995, ApJ, 455, L135
McGaugh, S. S. 1991, ApJ, 380, 140
McLaughlin, B. M., & Bell, K. L. 2000, J. Phys. B At. Mol. Phys., 33, 597
Mendoza, C. 1983, in IAU Symp. 103, Planetary Nebulae, ed. D. R. Flower (Dordrecht: Reidel), 143
Mennickent, R. E., Pietrzyński, G., & Gieren, W. 2004, MNRAS, 350, 679
Mesa-Delgado, A., Esteban, C., & García-Rojas, J. 2008, ApJ, 675, 389
Mesa-Delgado, A., Esteban, C., García-Rojas, J., Luridiana, V., Bautista, M., Rodríguez, M., López-Martín, L., & Peimbert, M. 2009, MNRAS, 395, 855
Meyer, D. M., Jura, M., & Cardelli, J. A. 1998, ApJ, 493, 222
Modjaz, M., et al. 2008, AJ, 135, 1136
Mokiem, M. R., Martín-Hernández, N. L., Lenorzer, A., de Koter, A., & Tielens, A. G. G. M. 2004, A&A, 419, 319
Monteverde, M. I., Herrero, A., Lennon, D. J., & Kudritzki, R. P. 1996, A&A, 312, 24
Mouhcine, M. 2006, ApJ, 652, 277
Moustakas, J., & Kennicutt, R. C., Jr. 2006, ApJ, 651, 155
Muñoz-Mateos, J. C., Gil de Paz, A., Boissier, S., Zamorano, J., Jarrett, T., Gallego, J., & Madore, B. F. 2007, ApJ, 658, 1006
Nagao, T., Maiolino, R., & Marconi, A. 2006, A&A, 459, 85
Oliveira, C. M., Dupuis, J., Chayer, P., & Moos, H. W. 2005, ApJ, 625, 232
Osterbrock, D. E., & Dufour, R. J. 1973, ApJ, 185, 441
Osterbrock, D. E., Fulbright, J. P., Martel, A. R., Keane, M. J., Trager, S. C., & Basri, G. 1996, PASP, 108, 277
Pagel, B. E. J., Edmunds, M. G., Blackwell, D. E., Chun, M. S., & Smith, G. 1979, MNRAS, 189, 95
Pannuti, T. G., Duric, N., Lacey, C. K., Goss, W. M., Hoopes, C. G., Walterbos, R. A. M., & Magnor, M. A. 2000, ApJ, 544, 780

Panter, B., Jimenez, R., Heavens, A. F., & Charlot, S. 2008, MNRAS, 391, 1117
Paturel, G., Petit, C., Prugniel, P., Theureau, G., Rousseau, J., Brouty, M., Dubois, P., & Cambrésy, L. 2003, A&A, 412, 45
Pauldrach, A. W. A., Hoffmann, T. L., & Lennon, M. 2001, A&A, 375, 161
Payne, J. L., Filipović, M. D., Pannuti, T. G., Jones, P. A., Duric, N., White, G. L., & Carpano, S. 2004, A&A, 425, 443
Peña, M., Stasińska, G., & Richer, M. G. 2007, A&A, 476, 745
Peimbert, M. 1967, ApJ, 150, 825
Peimbert, A. 2003, ApJ, 584, 735
Peimbert, M., & Costero, R. 1969, Bol. Obs. Tonantzintla Tacubaya, 5, 3
Pérez-Montero, E., & Díaz, A. I. 2003, MNRAS, 346, 105
Pérez-Montero, E., & Díaz, A. I. 2005, MNRAS, 361, 1063
Pérez-Montero, E., Díaz, A. I., Vílchez, J. M., & Kehrig, C. 2006, A&A, 449, 193
Pérez-Montero, E., Hägele, G. F., Contini, T., & Díaz, A. I. 2007, MNRAS, 381, 125
Pérez-Montero, E., et al. 2009, A&A, 495, 73
Pettini, M., & Pagel, B. E. J. 2004, MNRAS, 348, L59
Pettini, M., et al. 2001, ApJ, 554, 981
Pietrzyński, G., Gieren, W., Fouqué, P., & Pont, F. 2001, A&A, 371, 497
Pietrzyński, G., Gieren, W., Fouqué, P., & Pont, F. 2002, AJ, 123, 789
Pilyugin, L. S. 2003, A&A, 397, 109
Pilyugin, L. S. 2007, MNRAS, 375, 685
Pilyugin, L. S., & Thuan, T. X. 2005, ApJ, 631, 231
Pilyugin, L. S., Thuan, T. X., & Vílchez, J. M. 2006, MNRAS, 367, 1139
Pilyugin, L. S., Vílchez, J. M., & Contini, T. 2004, A&A, 425, 849
Porter, R. L., Ferland, G. J., & MacAdam, K. B. 2007, ApJ, 657, 327
Przybilla, N., Nieva, M.-F., & Butler, K. 2008, ApJ, 688, L103
Puls, J., Urbaneja, M. A., Venero, R., Repolust, T., Springmann, U., Jokuthy, A., & Mokiem, M. R. 2005, A&A, 435, 669
Quireza, C., Rood, R. T., Bania, T. M., Balser, D. S., & Maciel, W. J. 2006, ApJ, 653, 1226
Ramsbottom, C. A., Bell, K. L., & Stafford, R. P. 1996, At. Data Nucl. Data Tables, 63, 57
Read, A. M., & Pietsch, W. 2001, A&A, 373, 473
Rix, S. A., Pettini, M., Leitherer, C., Bresolin, F., Kudritzki, R.-P., & Steidel, C. C. 2004, ApJ, 615, 98
Rolleston, W. R. J., Smartt, S. J., Dufton, P. L., & Ryans, R. S. I. 2000, A&A, 363, 537
Romaniello, M., et al. 2008, A&A, 488, 731
Rosolowsky, E., & Simon, J. D. 2008, ApJ, 675, 1213
Roussel, H., Gil de Paz, A., Seibert, M., Helou, G., Madore, B. F., & Martin, C. 2005, ApJ, 632, 227
Rubin, R. H., et al. 2008, MNRAS, 387, 45
Rudolph, A. L., Fich, M., Bell, G. R., Norsen, T., Simpson, J. P., Haas, M. R., & Erickson, E. F. 2006, ApJS, 162, 346
Russell, S. C., & Dopita, M. A. 1990, ApJS, 74, 93
Sabbadin, F., Minello, S., & Bianchini, A. 1977, A&A, 60, 147
Sandstrom, K. M., Peek, J. E. G., Bower, G. C., Bolatto, A. D., & Plambeck, R. L. 2007, ApJ, 667, 1161
Savaglio, S., et al. 2005, ApJ, 635, 260
Schaerer, D., Contini, T., & Pindao, M. 1999, A&AS, 136, 35
Schild, H., Crowther, P. A., Abbott, J. B., & Schmutz, W. 2003, A&A, 397, 859
Schild, H., & Testor, G. 1991, A&A, 243, 115
Schild, H., & Testor, G. 1992, A&A, 266, 145
Searle, L. 1971, ApJ, 168, 327
Seaton, M. J. 1979, MNRAS, 187, 73P
Sérsic, J. L. 1966, Z. Astrophys., 64, 212
Shapley, A. E., Erb, D. K., Pettini, M., Steidel, C. C., & Adelberger, K. L. 2004, ApJ, 612, 108
Shaver, P. A., McGee, R. X., Newton, L. M., Danks, A. C., & Pottasch, S. R. 1983, MNRAS, 204, 53
Shaw, R. A., & Dufour, R. J. 1995, PASP, 107, 896
Shi, F., Zhao, G., & Liang, Y. C. 2007, A&A, 475, 409
Shields, G. A. 1974, ApJ, 193, 335
Simón-Díaz, S., Herrero, A., Esteban, C., & Najarro, F. 2006, A&A, 448, 351
Simón-Díaz, S., & Stasińska, G. 2008, MNRAS, 389, 1009
Smartt, S. J., Crowther, P. A., Dufton, P. L., Lennon, D. J., Kudritzki, R. P., Herrero, A., McCarthy, J. K., & Bresolin, F. 2001, MNRAS, 325, 257
Smartt, S. J., & Rolleston, W. R. J. 1997, ApJ, 481, L47
Smith, L. J., Norris, R. P. F., & Crowther, P. A. 2002, MNRAS, 337, 1309
Soffner, T., Mendez, R. H., Jacoby, G. H., Ciardullo, R., Roth, M. M., & Kudritzki, R. P. 1996, A&A, 306, 9
Sofia, U. J. 2004, in ASP Conf. Ser. 309, Astrophysics of Dust, ed. A. N. Witt, G. C. Clayton, & B. T. Draine (San Francisco, CA: ASP), 393
Stasińska, G. 1978, A&A, 66, 257
Stasińska, G. 1982, A&AS, 48, 299
Stasińska, G. 1990, A&AS, 83, 501
Stasińska, G. 2005, A&A, 434, 507
Stasińska, G., Schaerer, D., & Leitherer, C. 2001, A&A, 370, 1
Stasińska, G., Tenorio-Tagle, G., Rodríguez, M., & Henney, W. J. 2007, A&A, 471, 193
Storey, P. J., & Hummer, D. G. 1995, MNRAS, 272, 41
Tayal, S. S. 2007, ApJS, 171, 331
Tayal, S. S., & Gupta, G. P. 1999, ApJ, 526, 544
Tikhonov, N. A., Galazutdinova, O. A., & Drozdovsky, I. O. 2005, A&A, 431, 127
Tremonti, C. A., et al. 2004, ApJ, 613, 898
Trundle, C., Dufton, P. L., Hunter, I., Evans, C. J., Lennon, D. J., Smartt, S. J., & Ryans, R. S. I. 2007, A&A, 471, 625
Trundle, C., Dufton, P. L., Lennon, D. J., Smartt, S. J., & Urbaneja, M. A. 2002, A&A, 395, 519
Trundle, C., & Lennon, D. J. 2005, A&A, 434, 677
Urbaneja, M. A., Herrero, A., Kudritzki, R.-P., Najarro, F., Smartt, S. J., Puls, J., Lennon, D. J., & Corral, L. J. 2005a, ApJ, 635, 311
Urbaneja, M. A., Kudritzki, R.-P., Bresolin, F., Przybilla, N., Gieren, W., & Pietrzyński, G. 2008, ApJ, 684, 118
Urbaneja, M. A., et al. 2005b, ApJ, 622, 862
van Dokkum, P. G. 2001, PASP, 113, 1420
Venn, K. A., McCarthy, J. K., Lennon, D. J., Przybilla, N., Kudritzki, R. P., & Lemke, M. 2000, ApJ, 541, 610
Vila Costas, M. B., & Edmunds, M. G. 1992, MNRAS, 259, 121
Vila Costas, M. B., & Edmunds, M. G. 1993, MNRAS, 265, 199
Vílchez, J. M. 1989, Ap&SS, 157, 9
Vílchez, J. M., & Pagel, B. E. J. 1988, MNRAS, 231, 257
Vílchez, J. M., Pagel, B. E. J., Díaz, A. I., Terlevich, E., & Edmunds, M. G. 1988, MNRAS, 235, 633
Vlajić, M., Bland-Hawthorn, J., & Freeman, K. C. 2009, ApJ, 697, 361
Walcher, C. J., Böker, T., Charlot, S., Ho, L. C., Rix, H.-W., Rossa, J., Shields, J. C., & van der Marel, R. P. 2006, ApJ, 649, 692
Webster, B. L., & Smith, M. G. 1983, MNRAS, 204, 743
Yin, S. Y., Liang, Y. C., Hammer, F., Brinchmann, J., Zhang, B., Deng, L. C., & Flores, H. 2007, A&A, 462, 535
Zaritsky, D., Kennicutt, R. C., Jr., & Huchra, J. P. 1994, ApJ, 420, 87